Distribution of UV radiation at the Earth's surface from TOMS-measured UV-backscattered radiances

J. R. Herman,[1] N. Krotkov,[2] E. Celarier,[3] D. Larko,[2] and G. Labow[2]

Abstract. Daily global maps of monthly integrated UV-erythemal irradiance (290–400 nm) at the Earth's surface are estimated using the ozone amount, cloud transmittance, aerosol amounts, and surface reflectivity from the solar UV radiation backscattered from the Earth's atmosphere as measured by the total ozone mapping spectrometer (TOMS) and independently measured values of the extraterrestrial solar irradiance. The daily irradiance values at a given location show that short-term variability (daily to annual) in the amount of UV radiation, 290–400 nm, reaching the Earth's surface is caused by (1) partially reflecting cloud cover, (2) haze and absorbing aerosols (dust and smoke), and (3) ozone. The reductions of UV irradiance estimated from TOMS data can exceed $50 \pm 12\%$ underneath the absorbing aerosol plumes in Africa and South America (desert dust and smoke from biomass burning) and exceeded $70 \pm 12\%$ during the Indonesian fires in September 1997 and again during March 1998. Recent biomass burning in Mexico and Guatemala have caused large smoke plumes extending into Canada with UV reductions of 50% in Mexico and 20% in Florida, Louisiana, and Texas. Where available, ground-based Sun photometer data show similar UV irradiance reductions caused by absorbing aerosol plumes of dust and smoke. Even though terrain height is a major factor in increasing the amount of UV exposure compared to sea level, the presence of prolonged clear-sky conditions can lead to UV exposures at sea level rivaling those at cloudier higher altitudes. In the equatorial regions, $\pm 20°$, the UV exposures during the March equinox are larger than during the September equinox because of increased cloudiness during September. Extended land areas with the largest erythemal exposure are in Australia and South Africa where there is a larger proportion of clear-sky days. The large short-term variations in ozone amount which occur at high latitudes in the range $\pm 65°$ cause changes in UV irradiance comparable to clouds and aerosols for wavelengths between 280 nm and 300 nm that are strongly absorbed by ozone. The absolute accuracy of the TOMS monthly erythemal exposure estimates over a TOMS field of view is within $\pm 6\%$, except under UV-absorbing aerosol plumes (dust and smoke) where the accuracy is within $\pm 12\%$. The error caused by aerosols can be reduced if the height of the aerosol plume is more accurately known. The TOMS estimated irradiances are compared with ground-based Brewer spectroradiometer data obtained at Toronto, Canada. The Brewer irradiances are systematically 20% smaller than TOMS irradiance estimates during the summer months. An accounting of systematic errors brings the Brewer and TOMS irradiances into approximate agreement within the estimated instrumental uncertainties for both instruments.

1. Introduction

The global coverage afforded by satellite observations of UV irradiance, or flux density (energy per unit area per unit time), can be used to distinguish regional and global changes in contrast to purely local observations from ground-based instruments. Satellite estimates of UV irradiance are based on measurements using a single well-calibrated instrument over extended periods (1979 through 1992 and August 1996 through the present), so regional and temporal differences arising from instrumental errors are minimized. Unlike the direct ground-based irradiance measurements, satellite-derived UV-irradiance estimates are inferred from measurements of back-scattered radiation from the atmosphere and radiative transfer calculations. In the case of TOMS (total ozone mapping spectrometer) the measurements consist of the solar radiation scattered back from the atmosphere in six wavelength channels and a measurement of the extraterrestrial solar radiance in the same six wavelength channels. The information in the 6 wavelength channels is converted into ozone amounts, aerosol amounts, SO_2 amounts, scene reflectivity, and cloud transmittance. The combined derived data sets, along with Rayleigh-scattering coefficients [*Bates*, 1984], laboratory ozone absorption coefficients [*Bass and Paur*, 1985], and measured high-resolution extraterrestrial solar irradiance spectra [*Breuckner*, 1993], are sufficient to estimate UV irradiances at the surface at the time of the satellite overpass (between 1040 and 1200 LT, for Nimbus 7/TOMS (N7/TOMS), 1978–1993, and approximately 1100 LT for Earth-Probe/TOMS (EP/TOMS), August

[1]Laboratory for Atmospheres, Goddard Space Flight Center, Greenbelt, Maryland.
[2]Raytheon ITSS Corporation, Lanham, Maryland.
[3]Software Corporation of America, Beltsville, Maryland.

1996 to present). UV-irradiance estimates are obtained for areas corresponding to the satellite's field of view (FOV) on the Earth's surface ($150 \times 100 >$ FOV $> 50 \times 50$ km^2 for N7/TOMS and $99 \times 52 >$ FOV $> 38 \times 38$ km^2 for EP/TOMS, August 1996 to December 1997, and $60 \times 33 >$ FOV $> 26 \times 26$ km^2 for EP/TOMS, January 1998 to present) and depend on average atmospheric properties within that FOV. Since the TOMS orbit is Sun synchronous, the fields of view can be combined into a global map of the UV irradiance at the same solar time every day. Because of the accurate in-flight calibrations and stability of the instrument, the TOMS satellite estimates of UV irradiance are able to maintain absolute and relative accuracy over wide geographic areas and long periods of time [*Herman et al.*, 1991; *McPeters et al.*, 1996].

The accuracy of a particular day's UV exposure (time-integrated irradiance) at a specified location is limited by the coarse spatial resolution of the TOMS observations and the ability to obtain only one UV-irradiance estimate per day at the location. This is mostly because of the highly variable nature (temporal and spatial) of cloud and aerosol cover. When comparisons are made with ground-based measurements of UV irradiance, the satellite estimations should be integrated over periods of at least 1 week to average the effects of different views of clouds, aerosols, and ozone variability.

Estimates of the global distribution of UV irradiance have been discussed in previous papers [e.g., *Green*, 1983]. The most recent of these combined TOMS ozone values with cloud coverage obtained from ERBE (Earth Radiation Budget Experiment, 1985–1990) to produce a UV irradiance climatology [*Lubin et al.*, 1998]. This is an extension of techniques for satellite estimation of UV irradiance discussed by *Lubin and Jensen* [1995, 1997] and *Frederick and Lubin* [1988]. A UV-mapping effort using AVHRR data for clouds and GOME data for ozone values is described by *Meerkotter et al.* [1997]. TOMS ozone data have been used for UV irradiance mapping neglecting cloud effects [*Madronich*, 1993] and extended to include cloud effects estimated directly from TOMS [*Eck et al.*, 1987, 1995] using a simplified model of cloud transmittance.

This paper discusses the geographical distribution of UV irradiance over the Earth's surface, including the effects of clouds and aerosols (smoke, dust, and non-UV-absorbing haze) entirely derived from total ozone mapping spectrometer (TOMS) backscattered radiances and the ATLAS-3 SUSIM (space shuttle Atlas-3 Solar Ultraviolet Spectral Irradiance Monitor) extraterrestrial irradiances. UV irradiances are estimated from the derived quantities, ozone amount [*McPeters et al.*, 1996], cloud-haze-aerosol reflectivity [*Krotkov et al.*, 1998, 1999], absorbing aerosol optical depth [*Herman et al.*, 1997; *Torres et al.*, 1998], and surface reflectivity [*Herman and Celarier*, 1997]. We limit the irradiance estimates to 65°S to 65°N with emphasis on snow-free conditions. Comparisons between TOMS and Toronto Brewer-14 irradiance measurements are discussed in terms of expected errors and differences between the two types of measurements. Error estimates for UV irradiances obtained from TOMS data are discussed.

2. Estimation of UV Surface Irradiances

The simplest realistic optical model for estimating UV irradiance at the Earth's surface (280–400 nm) consists of a Rayleigh-scattering atmosphere combined with stratospheric and tropospheric absorption of UV-B solar radiance (280–320 nm) by ozone over a weakly reflecting (2–8%) surface [*Herman and*

Celarier, 1997]. This is the clear-sky, snow/ice-free case over land and oceans. There are minor daily variations (3–4%) in the apparent clear-sky surface reflectivity, which arise from the very frequent presence of ground haze. Usually, the UV-irradiance values obtained for clear-sky conditions form the upper envelope of measured daily values. An exception occurs for specialized conditions of exposure to direct sunlight plus sunlight scattered from clouds, which can increase the local UV irradiance over clear-sky values. Over a larger area the presence of clouds always reduces the area-integrated UV irradiance relative to clear-sky conditions.

The surface UV irradiance is estimated from the extraterrestrial solar irradiance obtained from ATLAS-3 SUSIM and TOMS backscattered radiance data using tables generated from the plane-parallel multiple-scattering radiative transfer program [*Dave*, 1964; *Dave and Gazdag*, 1970]. The tables include the effects of terrain height, solar zenith angle, ozone absorption, Rayleigh scattering, aerosol scattering and absorption, 340–380 nm surface reflectivity, and a pseudospherical geometry correction (spherical geometry for the unattenuated solar beam and for first-order scattering, with plane-parallel geometry for higher-order scattering). The pseudospherically corrected Dave model and the *Herman et al.* [1980] Gauss-Seidel model were compared with a full spherical geometry calculation [*Herman et al.*, 1996] and agree to within 1% up to solar zenith angles of about 83°.

2.1. Extraterrestrial Solar Irradiance

The ATLAS-3 SUSIM data (110–410 nm with 0.15 nm resolution) have been published on the Internet at the address http://wwwsolar.nrl.navy.mil/susim_atlas_data.html, and the corresponding lower spectral resolution Solar Stellar Irradiance Comparison Experiment (SOLSTICE) data are available from http://www-uars.gsfc.nasa.gov/cdrom_main.html. The ATLAS-3 SUSIM instrument was modified to be more accurate ($\pm 3\%$) than the ATLAS-1, ATLAS-2, and UARS versions of SUSIM. A general error analysis for the ATLAS-3 SUSIM data is not currently available, but for the previously measured spectrum (ATLAS-2 SUSIM), the accuracy was specified to be 4–8% [*Woods et al.*, 1996]. An example of the SOLSTICE and
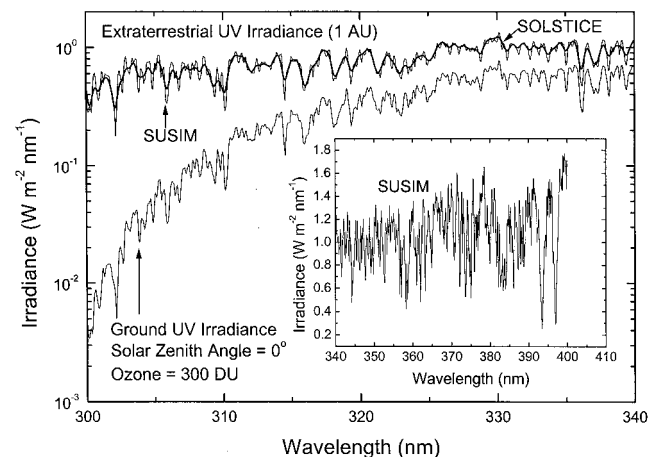

Figure 1. Atlas-3 SUSIM and UARS SOLSTICE solar irradiances at 1 a.u. showing the Fraunhofer line structure in the range 300–410 nm. The bottom curve is the calculated UV irradiance at the ground for SZA = 0°, and ozone amount = 300 DU.
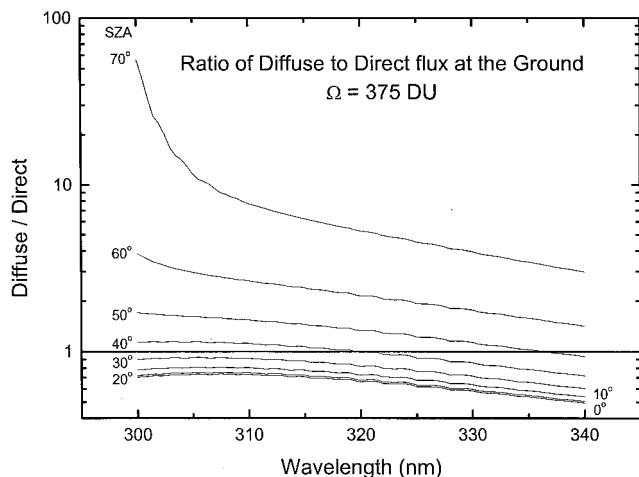
Figure 2. Ratio of diffuse irradiance to direct irradiance at the ground, Γ_0, as a function of wavelength (300–340 nm) and solar zenith angle (0°–70°). The ground pressure is assumed to be at 1 atm, and the surface reflectivity $R_S = 0$.

ATLAS-3 SUSIM data is shown in Figure 1 where the higher-resolution SUSIM data agree well with the SOLSTICE data. For the examples shown in Figure 1 the agreement is about 2% when the SUSIM data are degraded to SOLSTICE resolution. Either the 1992 SOLSTICE data or the 1994 SUSIM data can be used, since at the wavelengths of interest, 280–400 nm, the solar flux is invariant to within the precision of the measurements [*Lean et al.*, 1997]. Figure 1 shows the solar irradiance, containing the high-resolution Fraunhofer line structure, above the atmosphere, and the amount reaching the ground between 300 and 410 nm for overhead Sun in a clear-sky atmosphere containing 300 Dobson units (DU) of ozone.

The absolute accuracy of extraterrestrial radiance measurements is maintained through internal calibrations and data set intercomparisons (among SOLSTICE, SUSIM, and SBUV/2 instruments). *Cebula et al.* [1994, 1996] estimated the agreement between the UARS SUSIM and the SOLSTICE to be ±5% absolute. The measurements made by the two UARS instruments were compared with the same-day measurements by three other solar instruments (the solar spectrum (SOLSPEC), the shuttle solar backscatter ultraviolet (SSBUV), and the shuttle SUSIM instruments) during the ATLAS-1 and ATLAS-2 space shuttle missions in March 1992 and April 1993, respectively [*Cebula et al.*, 1996; *Woods et al.*, 1996], and ATLAS 3 in November 1994. In the 280–400 nm wavelength region, at 0.5 nm spectral resolution, the difference among the various data sets is less than ±3% and is wavelength dependent.

2.2. Clear-Sky UV Irradiance

Numerical solutions of the clear-sky radiative transfer equation have been tabulated for the expected range of atmospheric parameters (pressure, ozone amount, surface reflectivity, and solar zenith angle). These tables form an accurate numerical basis for estimating UV irradiance at the Earth's surface. The physical properties described in these tables are easily understood in terms of a formal solution of the radiative transfer equation for an absorbing and scattering atmosphere over a reflecting surface, as given by (1). Once the direct irradiance, $\mu_0 F$, is corrected for the Earth's spherical geometry and ozone absorption, the effects of atmospheric multiple

scattering are represented using the parameters Γ_0, R_S, and S_b obtained from numerical solutions of the pseudospherical plane parallel radiative transfer equation [*Dave*, 1965] for the Earth's clear-sky atmosphere (ozone absorption, Rayleigh scattering, and surface reflectivity). When the components Γ, R_S, and S_b are evaluated and combined into D_{IF}, the result is particularly simple to approximate with low-order polynomials (see Appendix) or tables. Aerosols and clouds are taken into account in a separate calculation.

The global (diffuse plus direct) UV irradiance on a horizontal surface at the ground, F_S, is given by

$$F_S = \mu_0 F[\tau(g)] \frac{(1 + \Gamma_0)}{(1 - R_S S_b)} = \mu_0 F[\tau(g)] D_{IF} \qquad (1)$$

where

$\Gamma_0 =$ ratio of diffuse to direct irradiance at the surface for $R_S = 0$. (See Appendix and Figure 2);

R_S Lambertian surface reflectivity (surface albedo typically 2–10%);

S_b fraction of radiation backscattered to the ground by the atmosphere (see Figure 3);

$\mu_0 F[\tau_g]$ direct irradiance at the ground at the optical depth $\tau(g)$;

D_{IF} diffuse irradiance factor, $(1 + \Gamma_0)/(1 - R_S S_b)$ (see Figure 4);

μ_0 cosine of the solar zenith angle, cos (SZA).

Figure 2 shows the ratio of diffuse irradiance to direct irradiance incident on the ground when the pressure is 1 atm. For SZA < 50°, Γ_0 is only weakly dependent on the stratospheric ozone amount but does depend on the amount and distribution of tropospheric ozone. When the diffuse to direct irradiance ratio $\Gamma(R_S)$ is evaluated for a realistic value of $R_S = 4\%$, $\Gamma(4)$ is almost unchanged from Γ_0.

Figure 2 shows that the diffuse component of the global (direct plus diffuse) irradiance is approximately equal to the direct component for SZA between 30° and 40° for the UV-B range and for SZA > 40° for the UV-A range (320–400 nm). At moderate to large solar zenith angles the majority of the UV irradiance at the Earth's surface is from the diffuse com-
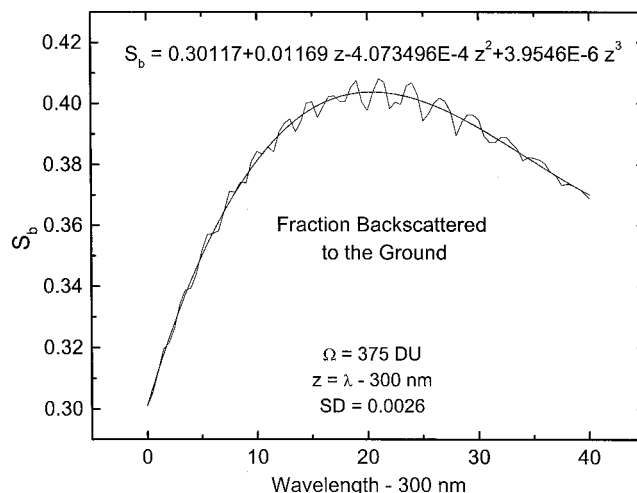

Figure 3. Fraction of radiation backscattered to the surface by the clear atmosphere, S_b. The smooth curve is a polynomial fit to S_b over the range 300–340 nm (see Appendix).
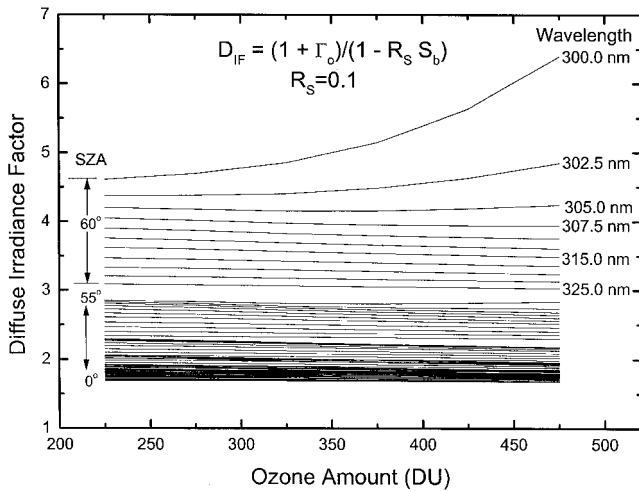
Figure 4. Diffuse irradiance factor, $D_{IF} = (1 + \Gamma_0)/(1 - R_s S_b)$, as a function of stratospheric ozone amounts, wavelength, and solar zenith angle (SZA). The wavelength range is from 300 to 325 nm and the SZA from 0° to 60° in steps of 10°. The 60° case is the top set of six curves. The remainder for SZA between 0° and 50° are contained in the lower group.

ponent. For example, these conditions are prevalent during the spring and autumn in the highly populated areas of Europe and North America above 40° latitude.

Figure 3 shows the fraction of radiation scattered back to the ground from the atmosphere in the absence of clouds. S_b peaks at about 40% near 320 nm because of ozone absorption at shorter wavelengths and reduced Rayleigh scattering at longer wavelengths. S_b is independent of the solar zenith angle and nearly independent of stratospheric ozone amounts but does depend on the ozone distribution and amount in the lower troposphere [see *Krotkov et al.*, 1998]. The small structure in S_b is from the ozone absorption coefficient. As is shown later, the amount of radiation scattered back to the surface depends strongly on the surface reflectivity, particularly when there is snow or ice, and on the presence of clouds.

The quantities Γ and S_b are combined as in (1) to form the diffuse irradiance factor $D_{IF} = (1 + \Gamma)/(1 - R_S S_b)$ shown in Figure 4. Here D_{IF} is plotted as a function of ozone amount from 200 to 450 DU and parametrically as a function of SZA and wavelength. For most conditions, D_{IF} is approximately independent of the amount of ozone in the atmosphere for SZA < 60° and wavelengths between 300 and 400 nm. As expected for the UV-A wavelengths longer than 325 nm, D_{IF} is almost independent of ozone amount for SZA up to 80°. This characteristic permits D_{IF} to be evaluated at a single ozone amount (e.g., 325 DU) and used for a variety of commonly occurring conditions. The values of D_{IF} in Figure 4 are suitable for use over land or ocean where R_s is less than 0.1, except when there is snow or ice, and can be computed from the fitting polynomials given in the Appendix.

Because D_{IF} is nearly independent of stratospheric and upper tropospheric ozone amounts for wavelengths between 300 nm and 400 nm, and a wide range of SZA, the perturbations in the global irradiance F_S caused by changes in ozone amount are proportional to the easily calculated changes in the direct irradiance at the Earth's surface $\mu_0 F[\tau_g]$. The radiative-transfer tables used to construct the solutions discussed in the

following sections cover a wider range of SZA, surface reflectivities, and wavelengths than shown for D_{IF}.

2.3. Reduction of UV Irradiance by Clouds

Large UV-irradiance variations come from changes in solar zenith angle (latitude and season) and the altitude above sea level. For a fixed location the largest cause of UV variability is caused by the presence of clouds and aerosols followed by smaller variations caused by ozone (wavelengths of 315 nm or smaller). This section and the ones following discuss the various sources of UV-irradiance variation relative to clear-sky conditions.

A simple model to account for the UV transmittance $T_{overcast}$ caused by pure water clouds in a Rayleigh-scattering atmosphere of transmittance T_{clear} over a low-reflectivity surface is based on an approximate energy balance using the measured scene reflectivity R_{380} from TOMS averaged over the satellite field of view (FOV) on the surface. There is a small correction to account for an average 5% surface reflectivity [*Eck et al.*, 1987, 1995; *Herman et al.*, 1996]. For this model, $CT = T_{overcast}/T_{clear} \approx CT_E = 1 - (R_{380} - 0.05)/0.9$ for $R_{380} \leq 0.5$ and $1 - R_{380}$ for $R_{380} > 0.5$ causes reductions in the amount of surface UV ranging from 0 to 100% over small geographical distances.

R_{380} is not the true scene albedo, since it does not account for the actual angular dependence of backscattered radiances. Instead, R_{380} is the Lambert equivalent scene reflectivity, LER, or the reflectivity of a Lambertian reflecting surface that causes the calculated radiance to equal the measured radiance. A slight generalization of the CT_E model is given by $1 - (R_{380} - R_G)/(1 - 2R_G)$, where R_G is from a reflectivity climatology [*Herman and Celarier*, 1997], typically 2–4% with small land areas and parts of the ocean having reflectivities near 8% (e.g., the southern Pacific Ocean gyre and parts of the Sahara Desert).

Using the CT_E model, *Eck et al.* [1995] showed an apparent agreement between the UV irradiances estimated from TOMS data with weekly averaged ground-based measurements at Toronto for a wide range of cloud conditions from spring to autumn. On a single very clear day (May 30, 1990), *Eck et al.* [1995] found that TOMS was less than the Brewer by about $1 \pm 2\%$ ($100[1 - B/T] = -1\%$) for all wavelengths between 300 and 325 nm. The lack of wavelength dependence in the difference implies that the correct amount of ozone was assumed in the model for May 30, 1997. When analyzing the data for April to November 1990, they found that the percentage difference between TOMS and Brewer was $10 \pm 2\%$ at 300 nm and $-4 \pm 2\%$ in the vicinity of 320 nm. The $14 \pm 3\%$ irradiance-error difference between 300 and 320 nm translates into an ozone error of $-4 \pm 1\%$ in the assumed amount of ozone.

In the current analysis for May 30, 1990, when $CT \approx CT_E \approx 1$, the TOMS estimated irradiance is greater than the Brewer-measured irradiance by 4.6%. However, the calibration of the Brewer irradiances was adjusted after the publication of *Eck et al.* [1995], so the new Brewer irradiance is 4% lower than the old irradiance measurements on May 30, 1990. Throughout 1990 the new calibration introduced changes that vary between $\pm 4\%$. The use of a new CT model [*Krotkov et al.*, 1999] increases the TOMS estimated irradiances relative to those estimated from CT_E by amounts that range from 5 to 40% depending on cloud amount, solar zenith angle, and the satellite zenith angle (see Figures 5 and 6). This causes the current analysis to disagree with that from *Eck et al.* [1995].

A better estimate of the cloud transmittance over the satellite FOV is given by a plane-parallel cloud attenuation model [*Krotkov et al.*, 1999], estimated from radiative transfer calculations. The results for 325 nm are shown in Figure 5 at the TOMS satellite zenith angle for nadir view $\eta = 0°$ and for the extreme off-nadir view $\eta = 62°$ for three SZA (0°, 46°, and 70°) and a solar azimuth view angle of 90°. The TOMS satellite zenith angle is the angle between the vector normal to the Earth's surface at the TOMS FOV and the vector from the TOMS FOV to the satellite. The full CT wavelength dependence caused by Rayleigh scattering and ozone absorption is described by *Krotkov et al.* [1999] and is used in this paper.

Figure 6 shows the percentage difference between the CT calculation and the $CT_E \approx CT_0 = 1 - R_{380}$. For nadir view, $CT > 1 - R_{380}$ for SZA between 0° and 50° except for thin clouds where it is approximately equal. For larger SZA, $CT < 1 - R_{380}$. For clouds that attenuate the 325 nm irradiance by about 50%, the CT is between 20 and 40% larger than $1 - R_{380}$ for SZA between 0° and 50° and about 10% less than $1 - R_{380}$ for SZA = 70°. For the full off-nadir view, $CT > 1 - R_{380}$ for almost all cloud thicknesses and SZA.

At Toronto the summertime noon SZA is greater than 19° near solstice and 27° at the TOMS overpass time of about 1100. Thus for the TOMS overpass time, CT is systematically greater than $1 - R_{380}$ for most of May, June, and July as is the UV irradiance estimated at the ground under a cloud layer. The differences range from 10 to 40% for all TOMS scan view angles for attenuation between 0 and 50%. Under optically thin clouds ($\tau < 1$) the estimated irradiance is only a few percent larger than predicted by $1 - R_{380}$.

For TOMS UV-irradiance estimates the cloud transmission factors CT are derived directly from the measured backscattered radiances at the long-wavelength TOMS channels (360 or 380 nm). For broken clouds it is assumed that the average CT properties over the TOMS FOV is the same as for the equivalent CT of a homogeneous cloud with the same scene

Figure 6. Percentage difference between the calculated CT for 325 nm and $1 - R_{380}$ at SZA = 0°, 46°, and 70° for TOMS satellite zenith angles at nadir view $\eta = 0°$ and off-nadir view $\eta = 62°$. Also shown are the equivalent plane-parallel cloud optical depths τ_{CL}. The dashed straight lines are guides connecting points of equal cloud optical depth.

reflectivity R. This assumption is currently being studied with Monte Carlo techniques.

2.4. Reduction of UV Irradiance by Aerosols

Reductions of UV irradiances can occur over large geographical regions underneath aerosol plumes associated with major dust storms and regions of biomass burning. In some cases (e.g., Indonesia smoke plumes with optical depth more than 5) the reduction estimated from TOMS data can be over 75%, but more often, the larger reductions amount to 50% or more [*Krotkov et al.*, 1998] as in cases of dust aerosols over the Sahara Desert during the summer months with optical depths of 2–3. When absorbing aerosols are included in the estimated UV-irradiance calculations, the absorbing aerosol layers are assumed to be geometrically thin layers (1 km) at ~3 km altitude. The aerosol-layer altitudes can be estimated from an analysis of the TOMS aerosol index and derived optical depths [*Herman et al.*, 1997; *Torres et al.*, 1998; *Hsu et al.*, 1999] by requiring equality with ground-based Sun photometer optical depths or determined directly from the few sites with ground-based lidar.

For absorbing aerosols the TOMS aerosol index A_I (formerly called residue) [*Herman et al.*, 1997] is approximately proportional to the aerosol optical depth τ_a, single-scattering coalbedo $1 - \omega$, and $1 - P/P_0$ (P is aerosol-plume pressure height for cloud-free FOV [*Torres et al.*, 1998; *Hsu et al.*, 1999], although with different proportionality factors for different types of aerosols such as dust, smoke (including industrial soot), volcanic ash, and nonabsorbing (e.g., industrially produced sulfates). The dependence on aerosol-plume height is not linear. A_I tends toward zero when the plume height falls below about 1.5 km and increases nearly linearly with height above 3 km [*Herman et al.*, 1997].

UV attenuation factors g can be derived for both the absorbing and the nonabsorbing aerosols in the absence of clouds [*Krotkov et al.*, 1998]. For absorbing aerosols an empirical attenuation equation that fits the radiative transfer results is
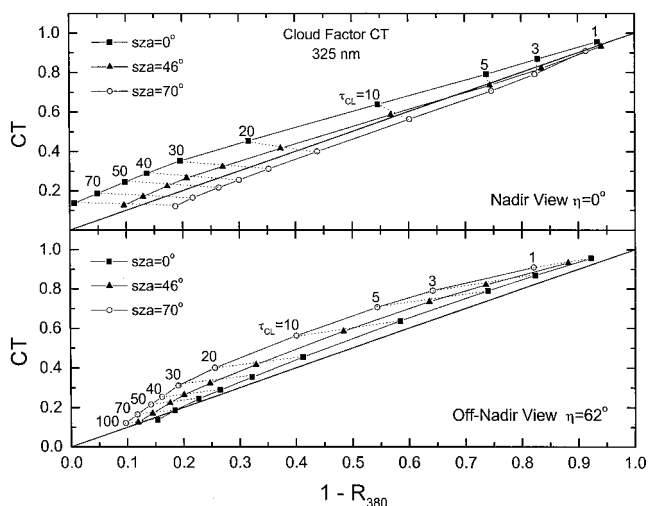

Figure 5. Cloud transmittance ratio $CT = T_{\text{overcast}}/T_{\text{clear}}$ as a function of the 380 nm Lambert equivalent reflectivity R_{380}, for SZA 0°, 46°, and 70° and satellite zenith angles for nadir view $\eta = 0°$ and full off-nadir $\eta = 62°$, derived from TOMS-measured backscattered radiance. Also shown are the equivalent cloud optical depths τ_{CL}. The dark straight line represents the case $CT = 1 - R_{380}$, and the dashed straight lines are guides connecting points of equal cloud optical depth.
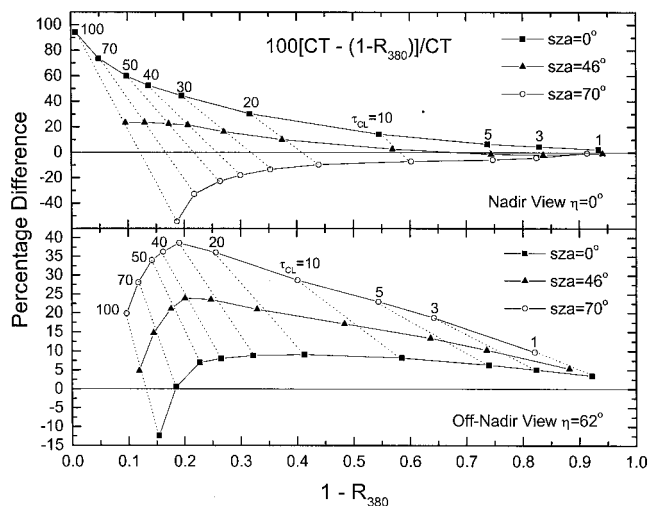
Table 1. Aerosol Parameters Used to Estimate Expected Errors E_F in UV-Irradiance Attenuation

Model/ Parameter	ω	k	S, km^{-1}	E_F, %
Smoke C1	0.92	0.25	12	±1.5
Smoke C2	0.84	0.37	40	±7.5
Dust D1	0.90	0.28	12	±1.7
Dust D2	0.72	0.50	43	±11
Dust D3	0.63	0.57	55	±16

$$F_A = F_S \exp\left[-gA_I\right] = F_S \exp\left[-k\tau_a\right] \quad (3a)$$

$$A_I = (k/g)\tau_a + O(\tau_a^2) + \text{constant} \ (-0.5 \text{ to } +0.1) \quad (3b)$$

where F_A is the reduced irradiance due to the presence of aerosols with aerosol index A_I relative to the clear-sky irradiance F_S. The linear relationship implied by (3b) has been investigated using Sun photometer data and TOMS overpass data for a variety of locations [see *Hsu et al.*, 1999, equation (3c)], and directly from radiative-transfer considerations [*Torres et al.*, 1998]. For optical depths greater than 2, the radiative transfer solutions show a small negative quadratic term added to (3b). The slope k/g in the linear relationship between τ_a and A_I varies with the type of aerosol and mostly depends on the single-scattering albedo and height of the aerosol plume (k/g increases with increasing absorption and plume height). The coefficient k depends most strongly on ω, while g depends on the aerosol plume height. For a Gaussian-shaped aerosol layer of thickness ±0.5 km located between 2 and 4 km altitude the factor g ranges between 0.2 and 0.3 for smoke or dust in the equatorial regions (SZA < 30°) [*Krotkov et al.*, 1998].

The empirical relationship between A_I and τ can be summarized using the average optical depths at 440 nm (dust) and 340 nm (smoke) from Sun photometer sites viewing dust and smoke compared with TOMS A_I values over the same sites [*Hsu et al.*, 1999],

$$A_I = 3.2\tau_{440} \ (k/g = 3.2 \pm 0.5 \text{ African dust,}$$

$$\text{summer, } \tau_{\max} = 1.5)$$

$$A_I = 1.3\tau_{440} \ (k/g = 1.3 \pm 0.1 \text{ African dust,}$$

$$\text{spring, } \tau_{\max} = 2.5)$$

$$A_I = 1.2\tau_{340} \ (k/g = 1.2 \pm 0.1 \text{ African smoke, } \tau_{\max} = 2)$$

$$A_I = 0.8\tau_{340} \ (k/g = 0.8 \pm 0.1 \text{ South American}$$

$$\text{smoke, } \tau_{\max} = 3.5)$$

(3c)

For the case of summer African dust, the high optical depths $\tau_{\max}$ measured by the Sun photometer are about 1–1.5 (corresponding to a measured 30–50% reduction in 440 nm direct beam solar irradiance) and the TOMS-measured A_I are about 3–4. For dust the optical depth at 440 nm is only slightly smaller than in the UV range (340–380 nm). For the dust model D2 (see Table 1) the optical depth coefficient is about 0.5, giving flux reductions of about $F_A = F_S e^{-(0.5)(1.5)} = 0.47$, or almost a 50% reduction in UV irradiance. Larger UV-irradiance reductions would occur in the spring when the optical depths are greater.

The following discusses error estimates in F_A/F_S. TOMS directly measures A_I, from which one can calculate the optical depth τ_a for a given type of aerosol if the altitude z is known from outside information [*Torres et al.*, 1998]. The sensitivity of optical depth determination to height errors depends on the aerosol type (refractive index, particle size distribution, and single-scattering albedo ω). For the five types of absorbing aerosols considered by *Torres et al.* [1998] (see Table 1) the altitude sensitivity $S = d\tau_a/dz$ (see (4)) for a given value of A_I at an assumed nominal altitude of ~3 km is shown in Table 1. From a fit to the radiative transfer solutions [*Krotkov et al.*, 1998] the corresponding values of $k \approx 0.1 + 2(1 - \omega) - 2(1 - \omega)^2$. The precise value of k varies with SZA and wavelength, but for error estimates in F_A/F_S, these nominal values are sufficient. From (3) the errors E_F in the estimated UV irradiance are given in Table 1 for an altitude uncertainty of ±0.5 km. Of these the D3 model represents the large-particle dust, which is only infrequently encountered for long-range transport in the atmosphere. See *Torres et al.* [1998] for a detailed description of the aerosol models D1, D2, D3, C1, and C2.

An estimate of the error in F_A/F_S can be made from

$$E_F = \frac{1}{F_A}\frac{dF_A}{dz} = -k\frac{d\tau_a}{dz} = -kS \quad (4)$$

For example, in the case of desert dust, the reduction in irradiance, $100(1 - F_A/F_S)$, frequently exceeds 50% with an uncertainty of about ±11%.

While k and the optical depth τ_a were used for the error analysis, the attenuation of UV radiation caused by aerosols is estimated directly from the measured aerosol index A_I and the height sensitive coefficient g.

Though the sensitivity to altitude error can be large for some aerosol models, comparisons of TOMS data with Sun photometer data, *Hsu et al.* [1999] and *Torres et al.* [1998] show that the derived optical depths agree for most cases when the altitude is assumed to be near 3 km. In addition, the small amount of scatter between the Sun photometer data and the TOMS data show that the altitudes of the aerosol plumes for specific locations and seasons are approximately repeatable.

3. Errors in Estimating UV Irradiance and Exposure

The UV irradiance at the Earth's surface estimated from TOMS backscattered radiance data is for a specific local time (~1100 for the current EP/TOMS) and is an average for conditions over the geographic extent of the TOMS footprint (average FOV for scan position 9 out of 36, 100 × 84 km^2 for N7/TOMS; 25 × 30 km^2 August 1996 to December 1997, and 45 × 38 km^2 December 1997 to present for EP/TOMS). Of equal interest is the exposure to UV irradiance integrated over extended periods (days to years). The TOMS estimated-daily exposure is likely to be quite different from the actual daily exposure experienced on the ground because of rapidly changing cloud and aerosol amounts over periods of minutes to hours. Because of this, only time-integrated, or time-averaged, quantities can be compared to ground-based measurements for validation over periods long enough (at least 1 week) to average out the effects of cloud and aerosol variability. Since the maximum daily irradiance occurs near noon, the TOMS 1100 estimate captures the cloud conditions near the time of the day contributing the most to the integrated exposure. The prob-

lems inherent in the TOMS-estimated irradiance can be easily seen when comparing a single UV-irradiance estimate from a TOMS overpass of a Brewer site.

Figure 7 shows an example of 1 day UV-irradiance data obtained at Toronto (Brewer 14) compared with TOMS-estimated UV irradiances. Shown in the figure are the clear-sky estimated irradiances (top smooth curve) and the irradiances for the TOMS-estimated amount of cloudiness at the time (1101 EST) of the Earth probe/TOMS overpass of Toronto (bottom smooth curve) on August 8, 1996. While the instantaneous agreement with the ground-based-measured irradiance appears reasonable, just minutes later, the actual irradiance is much larger than the satellite-estimated irradiance because of local changes in cloud conditions. Averaging the ground-based data over periods of a week or more reduces the effect of local variability in cloud and ozone amounts and makes the data more closely resemble the averages over the large TOMS footprint, unless there is a systematic bias in cloudiness or haze over the ground-observing site relative to regions 25–100 km distant.

An example of the daily variability of measured UV irradiances for both the TOMS and the Toronto single-monochromator Brewer 14 is shown in Figure 8. Brewer 14 has been selected because it has a long history of frequent careful calibrations and characterizations at the Environment Canada laboratory in Toronto [*Kerr and McElroy*, 1993; *Fioletov et al.*, 1997]. The Brewer data are obtained from the World Ozone and Ultraviolet Radiation Data Center in Toronto, Canada. The Brewer points are averages of irradiances measured at the TOMS overpass time ±30 min at Toronto for 1990. Shown in Figure 8 are single channels centered at 305 ± 0.5 and 324.5 ± 0.6 nm. The solid lines represent 7 day running averages for both the daily near-noon TOMS-estimated UV irradiances and the corresponding average Brewer irradiances. When the UV-irradiance data are averaged over a week, the result is good agreement for all types of sky conditions during the spring and autumn but not during the summer months. On average, during the summertime, TOMS-estimated irradiances are larger
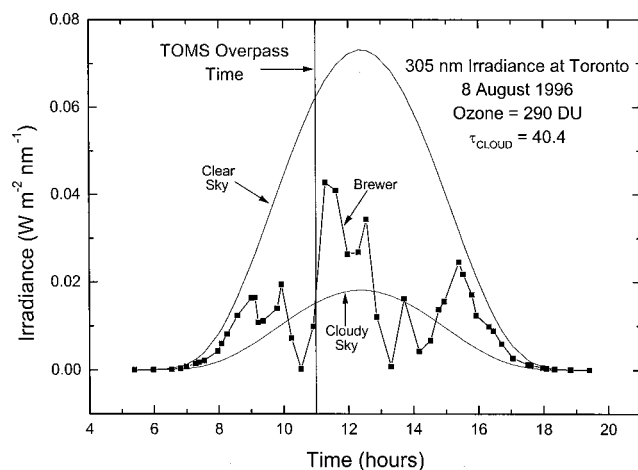

Figure 8. Comparison of the daily Toronto Brewer 14 data for single channels at 305 ± 0.25 and 324.5 ± 0.3 nm with TOMS UV-irradiance estimates at the TOMS overpass time ±30 min. The solid lines are weekly running averages.

by about 20% than those measured by the Brewer spectrophotometer.

The comparison differs from previous results [*Eck et al.*, 1995], which showed better agreement between the TOMS and the Brewer irradiances throughout most of the year. They found that the percentage difference between weekly averaged TOMS and Brewer measurements was about −4% (TOMS less than Brewer) for wavelengths longer than 315 nm where the ozone absorption is negligible. The differences in the current TOMS estimates of UV irradiance are mostly in the method used to estimate cloud transmittance (see Figure 5), where *Eck et al.* [1995] used $CT = [1 - (R_{380.} - 0.05)/0.90]R_{380} < 0.5$, the use of the previous version (version 6) of the TOMS ozone and reflectivity algorithm, and recalibrated TOMS data. The latter two represent small changes relative to the 20% difference, and all go to zero when considering the clear-sky long-wavelength comparison. The clear-sky case is a radiative-transfer calculation for a Rayleigh-scattering atmosphere with measured data used for the surface reflectivity and the extraterrestrial solar flux. Neither the ±3% error in the extraterrestrial solar irradiance nor the ±2% error in the surface reflectivity relative to their 5% estimate can account for the 20% differences.

3.1. Sources of Error

Possible causes of the disagreement between Brewer and TOMS irradiances are (1) small wavelength misalignments of the Brewer relative to the SUSIM-measured Fraunhofer line structure in the solar spectrum (see Figure 1), (2) underestimates (6%) for the Brewer irradiances caused by errors in the cosine weighting of the diffuser [*Bernhard and Seckmeyer*, 1997] estimated that such systematic errors could be more than 15% on some instruments), (3) overestimates of the TOMS irradiances caused by the presence of absorbing or nonabsorbing aerosols not detected by TOMS in the vicinity of Toronto by as much as 6% [*Krotkov et al.*, 1998], (4) surface reflectivity errors caused by the use of a climatology appropriate for the TOMS FOV (discussed below), (5) errors in the assumed ozone amount as derived from TOMS, which cause a wavelength-dependent error (see Table 2), (6) systematically un-

Figure 7. Comparisons between radiative-transfer-derived results (smooth curves) for clear and cloudy skies ($\tau_{CLOUD} = 40.4$ and ozone amount = 290 DU calculated from TOMS radiances) and corresponding ground-based measurements (squares) for August 8, 1996, at Toronto, Canada (Brewer 14 data from WOUDC database). The vertical straight line marks the 1101 EST of the Earth probe/TOMS overpass of Toronto.
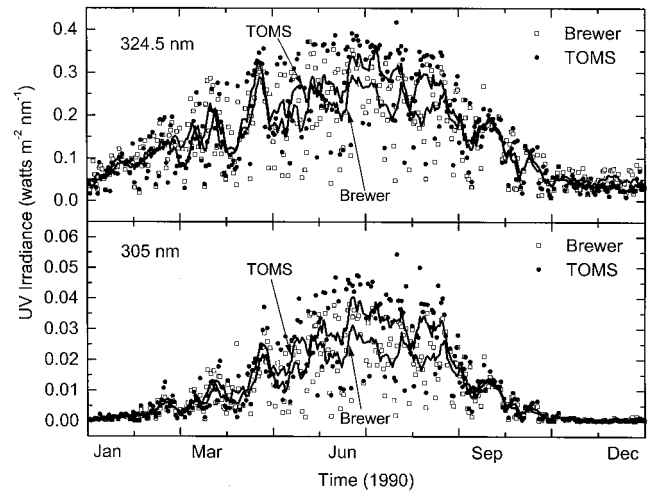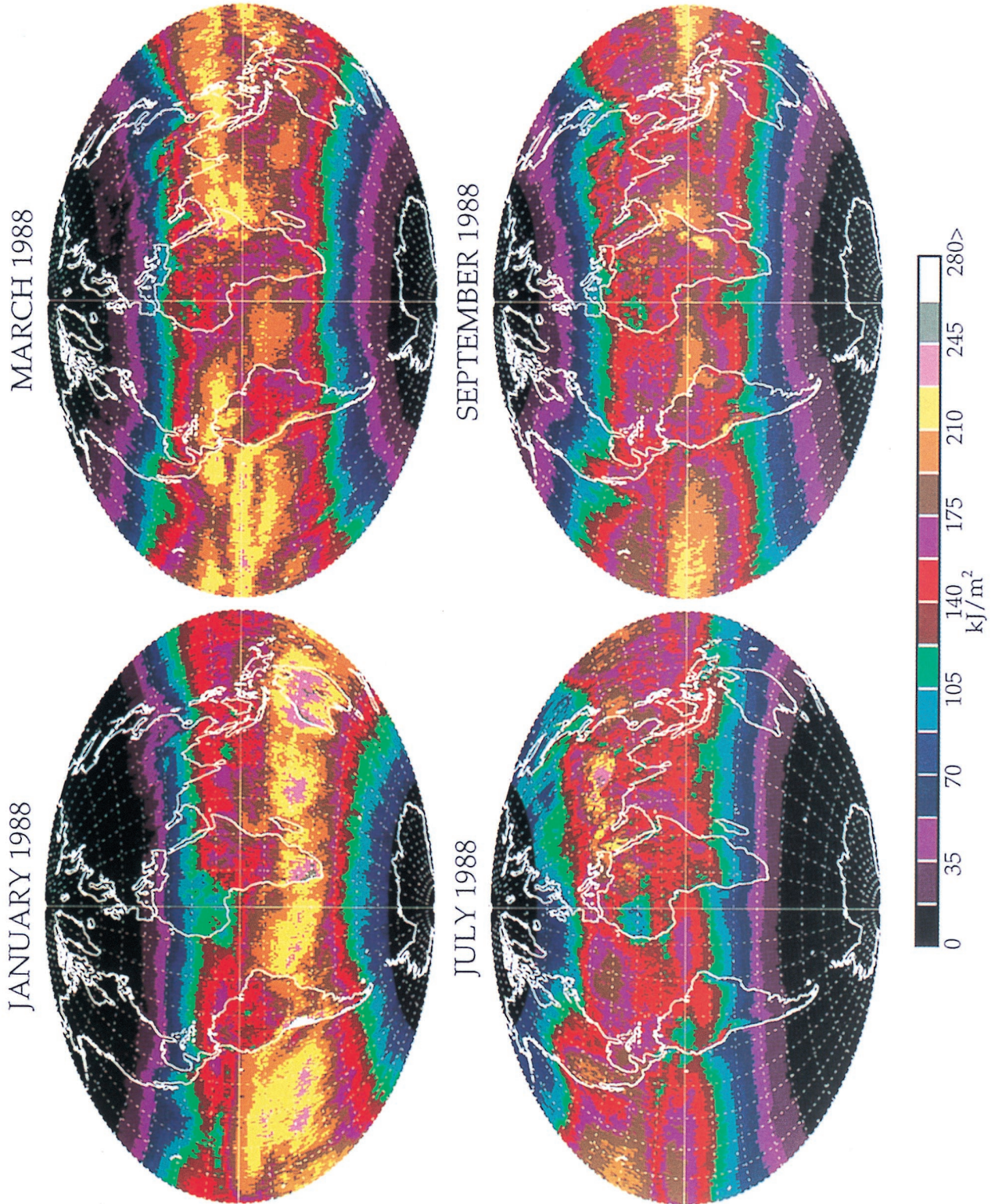
Plate 1. (a–d) Geographic distribution of monthly averaged UV irradiance from 290 to 400 nm weighted by the CIE erythemal action spectra. (a) January, (b) March, (c) July, and (d) September.
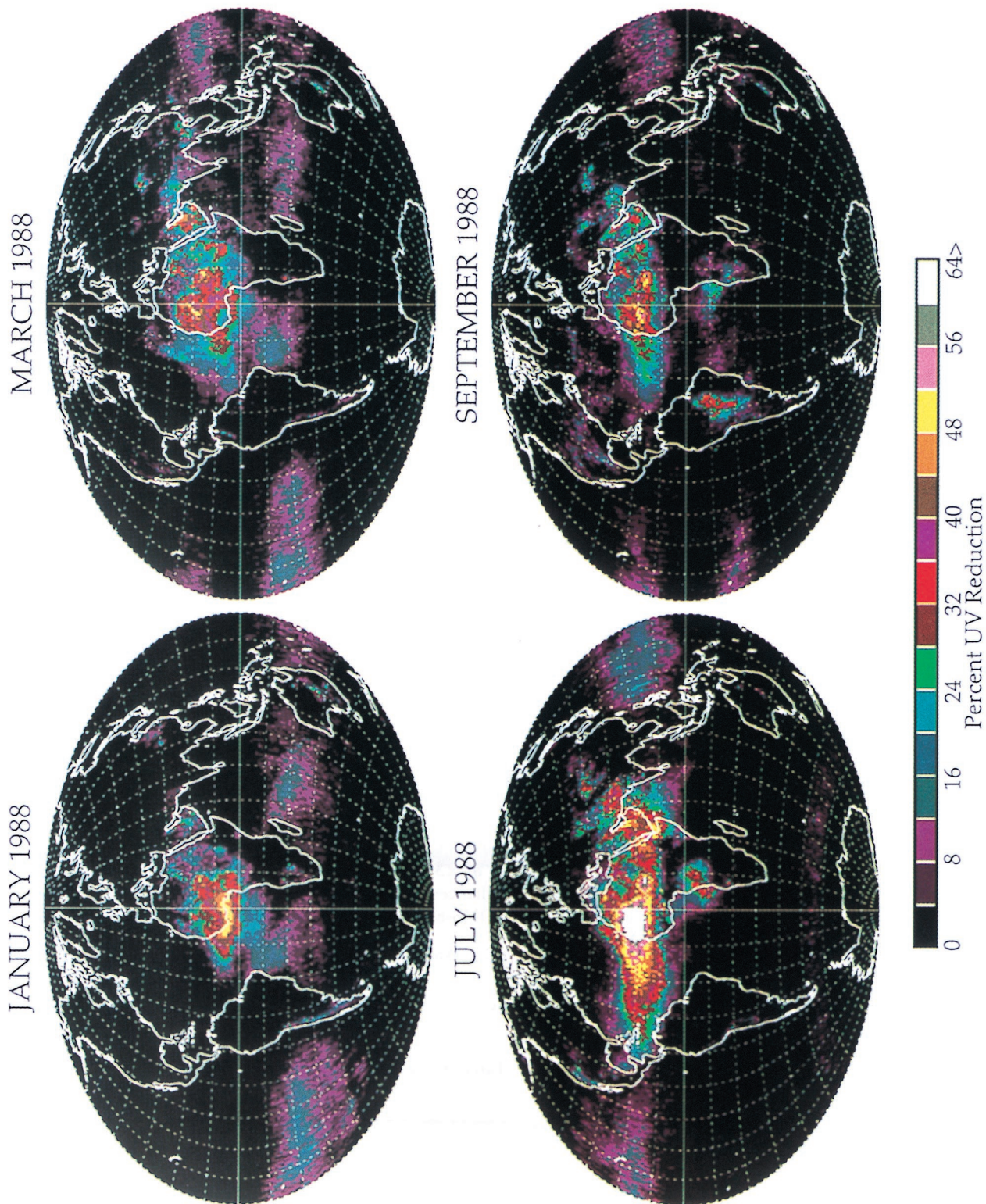
Plate 2. (a–d) Average reduction of UV exposure (in percent) by absorbing aerosols derived from equation (3) for the months of (a) January, (b) March, (c) July, and (d) September.

Earth Probe TOMS
UV Reduction due to Smoke over Indonesia for September 26, 1997
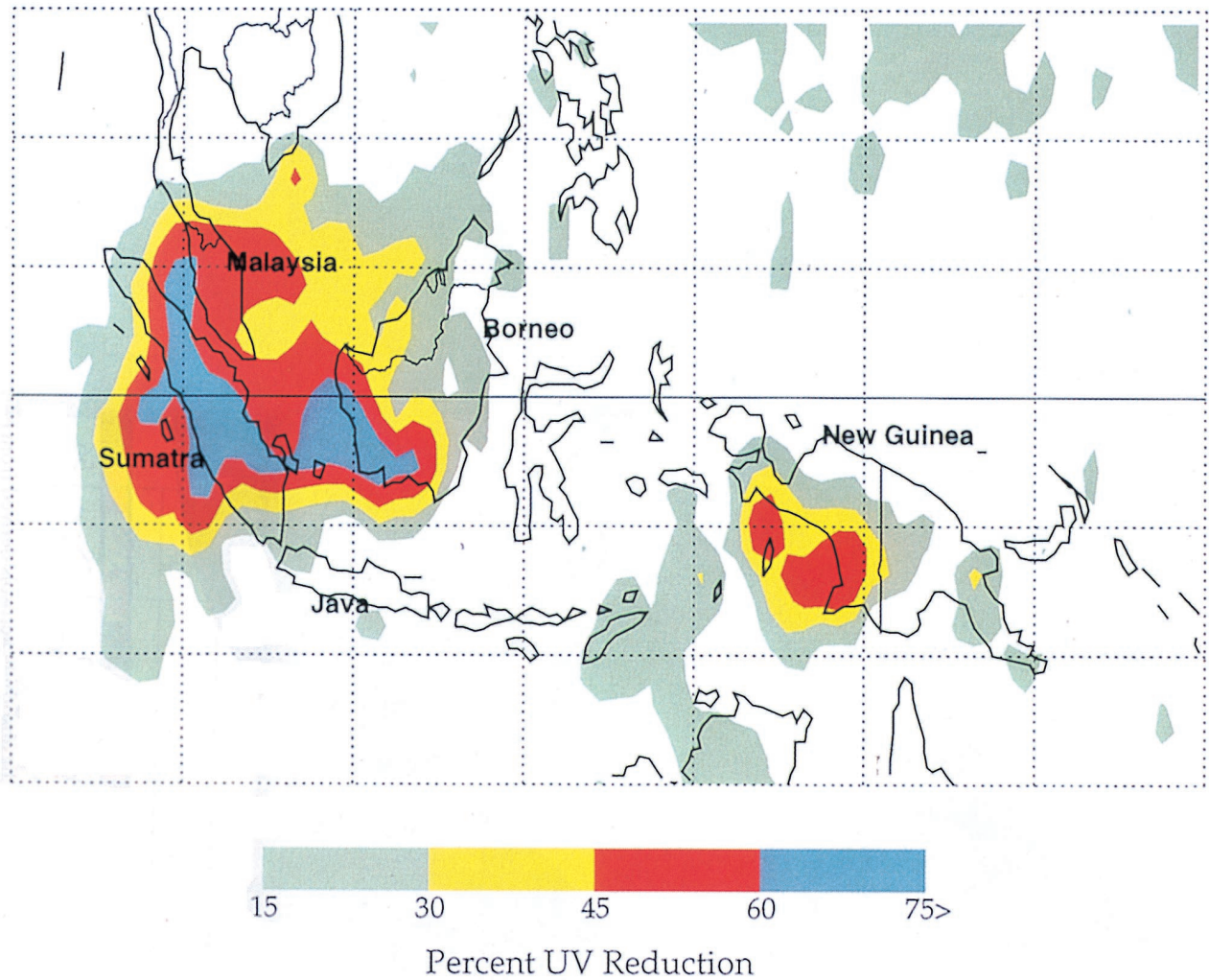

Percent UV Reduction

Plate 3.   Reduction of UV erythemal irradiance over Indonesia on September 23, 1997, from the presence of intense smoke plumes from biomass burning.

even distributions of clouds over Toronto compared with the average within the TOMS FOV (the size of this effect is unknown), (7) errors in the absolute radiometric calibration of either the Brewer (estimated at ±5%) or the TOMS (estimat-ed at ±3%) instruments, and (8) the use of the SUSIM solar radiances, with an estimated error of ±3%, to calculate the TOMS-estimated irradiance at the ground (see Table 3).

3.2.   Wavelength Errors

Combining adjacent Brewer channels to obtain irradiances over 5 nm bands should mostly eliminate the possible wave-

Table 2. $\alpha\Omega$ = Percent Decrease in Irradiance for a 1% Increase in Ozone Amount ($\theta = 0$)

Wavelength, nm	Percentage Change		
	275 DU	375 DU	475 DU
290	10.1	13.6	17.3
295	5.5	7.3	9.3
300	2.8	3.7	4.7
302.5	2.0	2.7	3.4
305	1.4	1.8	2.3
310	0.71	0.91	1.15
312.5	0.51	0.66	0.83
315	0.36	0.46	0.58
320	0.23	0.31	0.40
325	0.14	0.17	0.22

Table 3.   TOMS Versus Brewer Error Estimates

	Instrument	Estimate
Urban ground haze (estimated)	TOMS too high	3 ± 1%
Omitted absorbing aerosol	TOMS too high	8 ± 2%
Cosine error	Brewer too low	6 ± 2%
Slit function in model	TOMS too high	5%
Extraterrestrial flux	SUSIM	±3%
Ozone amount	TOMS	±2%
Scene reflectivity	TOMS	±1%
Radiometric calibration (in flight)	TOMS	±2%
Radiometric calibration	Brewer	±5%
Summary (TOMS-Brewer)	systematic 22%	±7%

length misalignment problem relative to the SUSIM-measured Fraunhofer line structure. As can be seen in Figure 9, this does not reduce the summertime difference. The sums of 10 adjacent Brewer channels have the same error as the individual channels shown in Figure 8, on average about 20% difference during the summer months (see Figure 9). The nearly uniform 20% disagreement at all summed wavelength channels rules out small-wavelength misalignments as the source of the differences.

The 20% disagreement is a persistent feature of the TOMS-Brewer comparison. In Figure 10 the 4 year average percentage difference, for all sky conditions, between TOMS and Brewer is about 20%, with the TOMS estimate of the Brewer irradiances about 13–16% too high and the Brewer irradiances 6% too low. For the period prior to about mid-March (about day 70) and after mid-November (about day 325) there are likely to be days with snow in the TOMS FOV causing TOMS to underestimate the surface irradiance. The underestimate is caused by the TOMS algorithm assuming that the enhanced reflectivity is entirely caused by clouds.

3.3. Cosine Weighting Errors

The total cosine error for Toronto-Brewer 14 is a 6% underestimate integrated over all directions (J. B. Kerr, personal communication, 1998) and are not included in the available data set from WOUDC. Cosine weighting errors would show a seasonal dependence since a larger percentage of the global (direct plus diffuse) UV irradiance is the direct Sun at a maximum SZA of 27° at summer solstice. The seasonal dependence does not account for the 20% summer difference.

3.4. Aerosol Errors

The presence of aerosols over Toronto is increased during the summer when stationary high-pressure systems dominate the weather over the eastern part of North America. Most of the time, the optical depths are small, and the reduction in irradiance over that estimated from TOMS data is 5–10%. The
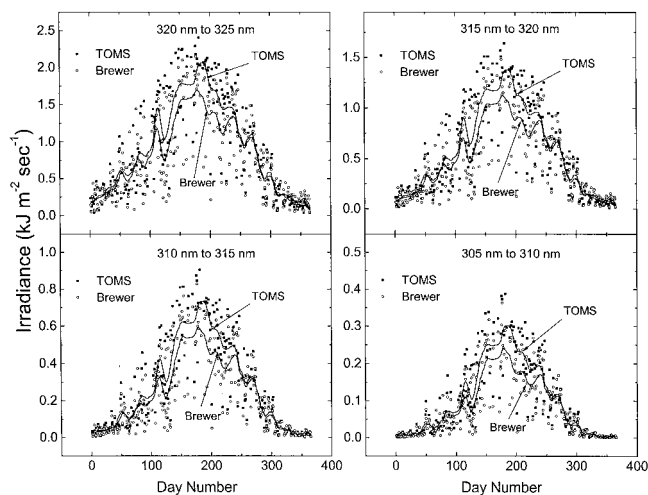

Figure 10. Percentage difference between the Toronto Brewer 14 (10 band sum, 320–324.5 nm) and TOMS for the average Brewer irradiance in ±30 min around the TOMS overpass time. The curve labeled "average" is the average of the four annual curves (1989–1992). Some of the larger percentage differences are labeled with the year of occurrence.

TOMS UV algorithm would detect the widespread presence of nonabsorbing aerosols as a scene with increased reflectivity and would reduce the surface UV according to the CT factor (see Figure 5). An error could occur if the aerosol optical depths in the vicinity of urban Toronto are higher than in adjacent less populated areas within the 100 km TOMS FOV. When UV-absorbing aerosols are present but not detected by TOMS, (e.g., the aerosols cover too small an area relative to the TOMS FOV, there is a small absorbing component within a sulfate aerosol plume, or the aerosols are below 1.5 km altitude, so TOMS would only see the scattering component), omitting the absorbing component of an aerosol would cause an overestimate of the TOMS irradiance.

Use of ground observations at Toronto for overhead aerosol amounts along with the UV irradiance measurements have been shown to improve the TOMS-Brewer comparisons by decreasing the percentage difference from an average 20% to an average of 8–10% on 30 cloud-free days [*Krotkov et al.*, 1998]. For these days the aerosol optical depth τ ranged from 0.2 to 1 with a single-scattering albedo of 0.95. For this type of aerosol the attenuation of the 323–325 nm UV irradiance was 4% ($\tau = 0.2$) to 18% ($\tau = 1$) with the largest number of points in the vicinity of 8 ± 2% ($\tau = 0.3–0.5$). When the Brewer cosine error is taken into account, it brings the clear-sky irradiances into agreement with those estimated from TOMS data.

Assuming that TOMS and the ground-based instrument are well calibrated and maintained, there are two additional sources of error inherent in the TOMS irradiance estimates, which have not been discussed. These are the surface reflectivity and ozone amounts used in the radiative transfer calculations. The assumed surface reflectivity is based on a climatology compiled from TOMS 380 nm backscattered radiances, and the ozone amount is estimated from triplets of TOMS backscattered radiances.

3.5. Surface Reflectivity Errors

Errors in the value of the assumed surface reflectivity usually lead to small errors in the estimated UV irradiance at the

Figure 9. Comparison of four summed 5 nm wide Brewer 14 channels with comparable irradiance estimates from TOMS. The points are daily data from 1989 averaged for the 1 hour surrounding the overpass time of 1100. The solid curves are a 7 day Fourier transform low-pass filter simulating a week's average of data for a data set with missing days (85 days missing out of 365).
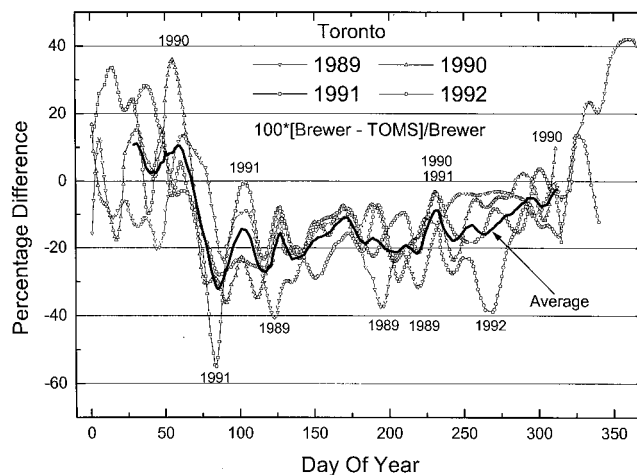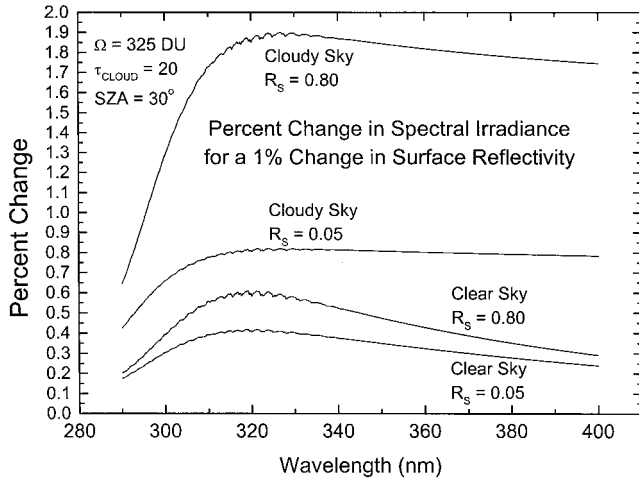
Figure 11. Changes is estimated UV irradiances for a unit change in surface reflectivity as a function of wavelengths for ground reflectance R_S = 0.05 and fresh-snow/ice conditions, R_S = 0.80 for clear and cloudy (τ_{cloud} = 20) skies with ozone amount Ω = 325 DU and SZA = 30°.

surface. This is because the reflectivity R_S < 0.1 enters into the formal solution of the radiative transfer equation in the form $[1 - S_b R_S]^{-1}$ (see (1) and Figure (3)). As seen in the two clear-sky curves in Figure 11, a 1% error in assumed surface reflectivity at 320 nm causes an error of a little more than 0.6% for snow-covered ground and about 0.4% for bare ground. However, the presence of clouds increases the amount of radiation reflected back to the ground and the error caused by an incorrectly assumed ground reflectivity. The error doubles for clouds over bare ground to about 0.8% and increases by a factor of 2.3(1.85%) for clouds over fresh snow. In the case of snow or ice, the uncertainties in the surface reflectivity can be quite large (new snow reflectivity 85–90%, old snow 50% or less, snow in an urban environment 10% or more). In summary, the estimated TOMS scene reflectivity error of ±1% leads to an additional ±0.5% irradiance error for clear skies and ±0.8% under cloudy skies for snow-free cases.

The reflectivity-minimum method used to obtain the reflectivity climatology [*Herman and Celarier*, 1997] for the Toronto pixel (average dimension, 100 km) would select the lower reflectivity values characteristic of the surrounding land areas instead of the higher reflectivity (about 2% higher) values of the nearby lake to characterize the ground reflectivity near Toronto. This error is not significant during the summer.

3.6. Ozone Errors

For the UV-irradiance relative error $\delta F/F \approx dF/F$ caused by small uncertainties in ozone amount, the error can be most easily estimated from the equation for the radiation amplification factor RAF, where α is the ozone absorption coefficient, Ω is the ozone amount, and θ is the SZA.

$$\frac{\delta F}{F} \approx -\alpha\Omega \frac{\delta\Omega}{\Omega} \sec(\theta) \quad (5)$$

$$\text{RAF} = -\frac{dF/F}{d\Omega/\Omega} \approx \alpha\Omega \sec(\theta) \quad (6)$$

For most conditions, the RAF (see Table 2 and Figure 12 for the θ = 30° case) can be estimated from $\alpha\Omega \sec(\theta)$, where $\theta <$

50°, or from radiative transfer calculations for any θ. Each pair of curves in Figure 12 shows a comparison between the RAFs from a full radiative transfer calculation and from (5). The top panel consists of three pairs of plots for three different ozone amounts (275, 375, and 475 DU). The bottom panel shows the absolute difference between each pair. The good agreement of the full radiative transfer calculation with (5) is because the scattering factor D_{IF} almost cancels when estimating the percentage change in UV irradiance for a small percentage change in total ozone (see Figure 4); that is, $dD_{IF}/d\Omega \approx 0$.

For larger θ and high ozone amounts, deviations from (6) can occur from the Umkehr effect [*Mateer*, 1965; *Fioletov et al.*, 1997]. The Umkehr effect occurs when the direct solar UV radiation at high solar zenith angles (near the horizon) is absorbed by ozone along the large slant path to the observer's site. In this case, the global radiation (scattered plus direct) consists of mainly diffuse radiation that scatters high in the atmosphere, above the ozone-density maximum, over the observers site. These scattered photons have a shorter optical path through the ozone than the photons in the direction of the direct beam and therefore a reduced RAF compared to the prediction of (5) and (6).

3.7. Irradiance Ratios

The seasonal dependence of the disagreement between TOMS and Brewer irradiances is mostly removed by forming the ratios of each 5 nm wide wavelength channel, λ = 292.5, 297.5, 302.5, 307.5, 312.5, 317.5 ± 2.5 nm, with the λ = 322.5 ± 2.5 nm channel. The remaining annual variability arises from the SZA dependence of the ozone absorption for the shorter wavelengths relative to 322.5 nm.

Some of the differences between the TOMS and the Brewer irradiance ratios with the 322.5 nm channel are due to the uncertainty in ozone amounts. Forming the percent difference between the TOMS and the Brewer ratios, TOMS is 9.6 ± 2.7% higher at the 302.5 nm ratio and is 2.4 ± 0.7% higher than the Brewer ratio at the 312.5 nm ratio (see Figure 13). If
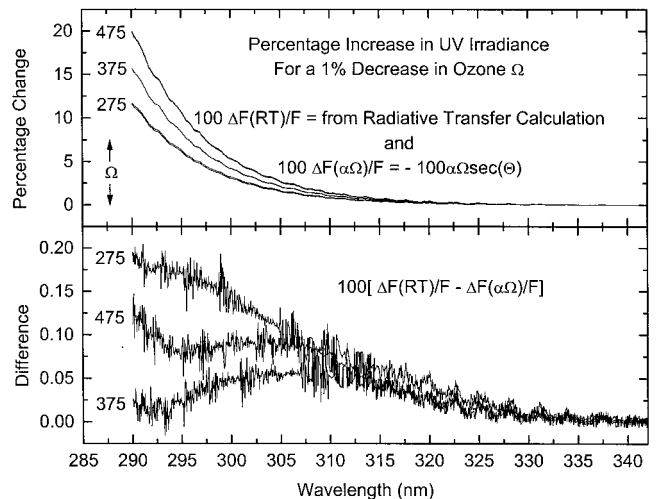

Figure 12. RAF for SZA = 30° as a function of ozone amount (Ω = 275, 375, and 475 DU) and wavelength calculated from increases in UV radiation due to a 1% reduction in ozone from a radiative-transfer calculation (three curves) and equation (5) (three curves). Value α is equal to the ozone absorption coefficient. The bottom panel shows the absolute difference between the closely matched pairs of curves.
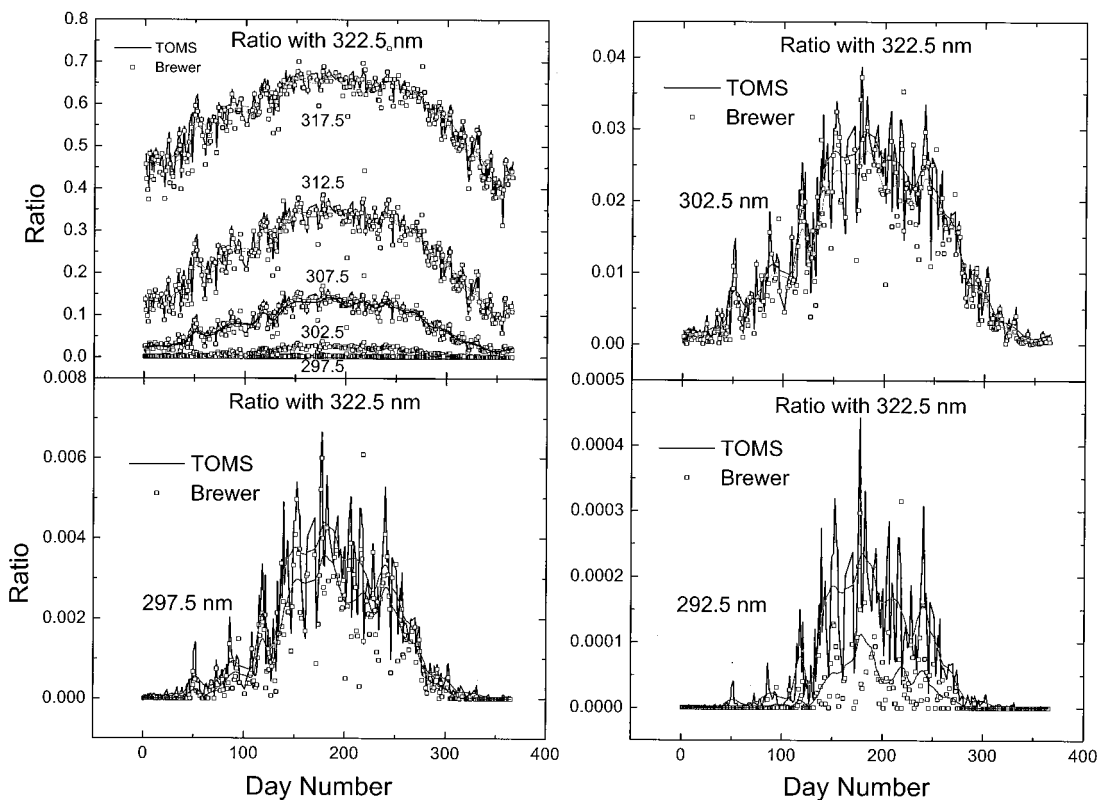
Figure 13. Irradiance ratios $I_\lambda/I_{322.5}$ for $\lambda = 292.5, 297.5, 302.5, 307.5, 312.5, 317.5 \pm 2.5$ nm. The Brewer data are plotted as open squares and the TOMS data as the vertices of solid lines.

all of the difference at the 302.5 nm ratio is due to ozone, then there would be a TOMS ozone underestimate of 2.8% relative to the local value at the Toronto Brewer site.

In general, for the estimation of uncertainties in the global distribution of UV irradiance, (5) can be used to estimate the TOMS UV-irradiance errors caused by the 2% uncertainty in TOMS-measured ozone amounts. For example, using (5) and Table 3 for 375 DU at $\theta = 45°$, the estimated 2% TOMS ozone uncertainty would lead to an uncertainty in the TOMS-estimated UV irradiance at 300 nm of 2(4.2)(1.4) = 12%, while at 310 nm, the uncertainty would be about 2(1.1)(1.4) = 3%. At longer wavelengths the ozone uncertainty has smaller effects, as shown in Figure 14.

3.8. Summary of Uncertainties

The disagreement between the TOMS and the Brewer spectroradiometer is mainly during the May to August period when there are more clear days (low TOMS reflectivity of less than 15%) than cloudy days on average. When the data are filtered for clear days as a function of TOMS estimated reflectivity, the differences are at a maximum (20%) for a scene reflectivity of 5% and decrease to about 12% for a scene reflectivity of about 2% (the ground reflectivity). The TOMS-Brewer difference decreases to zero at about 40% reflectivity and slightly reverses (−10%) for reflectivities greater than 40%. Weekly averages for all conditions differ by about 20%.

Table 3 summarizes the major errors, systematic and random, for the TOMS-Brewer intercomparison. The systematic errors consist of a possible undetected (by TOMS) urban ground haze, perhaps 3 ± 1%, in addition to that seen by TOMS in excess of the minimum ground reflectivity, the

Brewer cosine correction error of 6 ± 2% causing an underestimate of the irradiance, and a slit function shape error (assumed triangular) in the radiative transfer model causing an estimated 5% overestimate of the TOMS irradiance (adjusted for the Brewer slit function), when comparing with the Toronto Brewer 14, and a 8 ± 2% TOMS irradiance overestimate due to UV-absorbing aerosols not detected by TOMS.

For wavelengths between 300 and 325 nm the estimated systematic errors are about 22%, with TOMS higher than
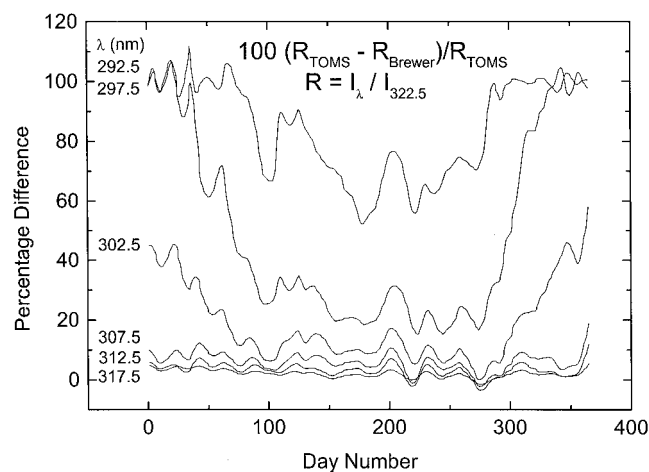

Figure 14. Percentage difference between the TOMS and the Brewer weekly average irradiance ratios. On day 190 the percent differences are 60, 21, 9.6, 4.6, 2.4, 1.2 for the wavelengths λ (nm) 292.5, 297.5, 302.5, 307.5, 312.5, 317.5, respectively.

Brewer, with the comparison having an accuracy of about ±7%. The cloudless-sky accuracy of TOMS estimates of surface irradiance is ±4% if the amount of absorbing aerosols are known. For regions where there are large reductions in UV irradiance caused by dust or smoke estimated from the TOMS A_I, the uncertainties are ±12% (combined uncertainty including average for dust and smoke). For wavelengths between 290 and 315 nm the uncertainty in ozone amount can cause increased uncertainty in the TOMS estimated irradiance.

Cloudless-sky Brewer irradiance ratios with the 324.5 nm irradiance obtained at Toronto have also been analyzed by *Krotkov et al*. [1998] and shown to agree with the TOMS-estimated irradiance ratios to within 5% for most wavelengths in the range from 300 to 325 nm and for SZA less than 60° even when aerosols are not taken into account. For SZA between 60° and 70° the errors can increase to about 8% between 300 and 305 nm. These errors are consistent with the above uncertainties for all sky conditions. Agreement between TOMS and Brewer irradiances was within 8% when aerosols were taken into account [*Krotkov et al*., 1998].

The large variation in the percentage difference between the TOMS and the Brewer during winter is probably due to changes in the amount cloudiness and the presence of snow/ice. The presence of clouds and snow/ice diminishes the relative importance of aerosols not detected by TOMS in reducing the UV irradiance. While there is significant production of aerosols during the cold months, there is little buildup of aerosol-polluted air from October to March due to the increased winds in the area compared to the summer months. In addition to removal of aerosols by wind, the percentage of cloudy days during the winter increases relative to the summer months. The cleaner air and increased cloudiness, and higher solar zenith angles (larger diffuse to direct irradiance ratio), removes most of the 11% aerosol systematic error associated with Toronto. Finally, the presence of snow on the ground will cause TOMS to underestimate the UV irradiance on both cloudy and cloud-free days, using the current algorithm.

When calculating the exposure to UV irradiance without reference to a Brewer instrument, the slit function and diffuser errors do not enter into the TOMS-estimated irradiances, leaving the TOMS systematic error as 3 ± 1% too high (undetected ground haze) with a statistical error of ±4% for UV-A and ±4.5% for 310 nm to ±9% for 300 nm irradiances. The statistical error for the erythemal irradiance is about ±4.5%. The presence of local absorbing aerosols, which are not detected by TOMS, could increase the TOMS-irradiance overestimate by about 8% (estimated at Toronto), usually at large urban locations. At present, the site-to-site variation of the local absorbing-aerosol reduction in UV irradiance is not known. There is an additional source of UV-B irradiance uncertainty based on the small difference between ozone values measured by N7/TOMS and EP/TOMS (about 1% higher) relative to the Dobson network.

4. Geographic Variability of UV Irradiance

In the following, most of the results are expressed in terms of UV exposure. The monthly erythemal exposure is defined as the time (1 month) and wavelength (290–400 nm) integrated UV irradiance striking a horizontal surface, weighted by an erythemal action spectrum (CIE action spectrum for erythema [*McKinlay and Diffey*, 1987] with an RAF due to ozone of about 1 in low and midlatitudes). The exposure units are given

as kJ/m² by assuming that the action spectrum is dimensionless, having been normalized to 1 at a specified reference wavelength.

The discussion concerns the variability of UV exposures caused by changes in the amount of cloudiness, aerosol amount, short-term ozone amount, season, and altitude. Long-term UV-irradiance changes [*Herman et al*., 1996], caused by gradually decreasing ozone amounts will not be considered here, since they are much smaller than irradiance variations caused by clouds, SZA, and aerosols that lead to most of the geographic and seasonal differences. Because of the difficulties of separating snow and cloud effects, the latitude range was limited to areas mostly free of snow and ice during spring, summer, and autumn months (±65°).

Plates 1 to 4 show the global distribution of 1 month's erythemal UV exposure for near-solstice conditions (January and July 1992) and near-equinox conditions March and September 1992), including both cloud and aerosol reductions. Geographic areas whose latitudes are near the monthly subsolar points (±23°) produce very high surface UV radiation over many areas of the world (South Africa, Sahara, Middle East, India, China, southwestern United States, South and Central America). For the scale used in the figures, pink and grey represent levels of UV erythemal exposure which are likely to cause burning of unprotected skin in many individuals over relatively short periods of time and where longer-term exposure can cause cataract disease in eyes and the induction of skin cancers [*United Nations Environmental Programme (UNEP)*, 1994]. For susceptible individuals, prolonged exposure at lower levels of UV irradiance may also cause health problems. Even higher levels of UV radiation, indicated by white areas, are generally associated with higher altitude, relatively cloud-free regions, such as in the Andes and Himalaya Mountains.

For most regions with very high year-to-year UV-exposure levels (latitude range, ±30°), there has been no significant long-term change in ozone amounts, and therefore no long-term significant ozone-related change in UV irradiance. Only South America, among the regions with major absorbing aerosol production, has shown a significant long-term change (increase) in aerosol amount on top of interannual variability [*Herman et al*., 1997]. There are smaller increases observed (1980–1992) in aerosol amounts in other regions, but the increases are of the same order as the interannual variability. Zonally averaged scene reflectivities (cloud transmittance) have not changed since 1979 [*Herman et al*., 1996] though there have been regional changes in reflectivity. The general characteristics of the UV distribution over the Earth's surface is well represented by any year's data obtained from TOMS. For this discussion, 1988 was chosen since the South American amount of biomass burning was fairly large compared to earlier years.

Summer: In January (see Plate 1a) during the Southern Hemisphere summer, most of South Africa has large regions labeled pink and grey because of the nearly overhead Sun over a moderately elevated and cloud-free region. From the presence of high-exposure regions over the oceans, it is clear that the lack of clouds over an extended period of time result in exposures that are comparable to those at moderate altitudes above sea level. As expected, large portions of Australia are subject to very high exposure levels both because of its nearness to the equator and because of the high frequency of occurrence of clear days. For the corresponding conditions
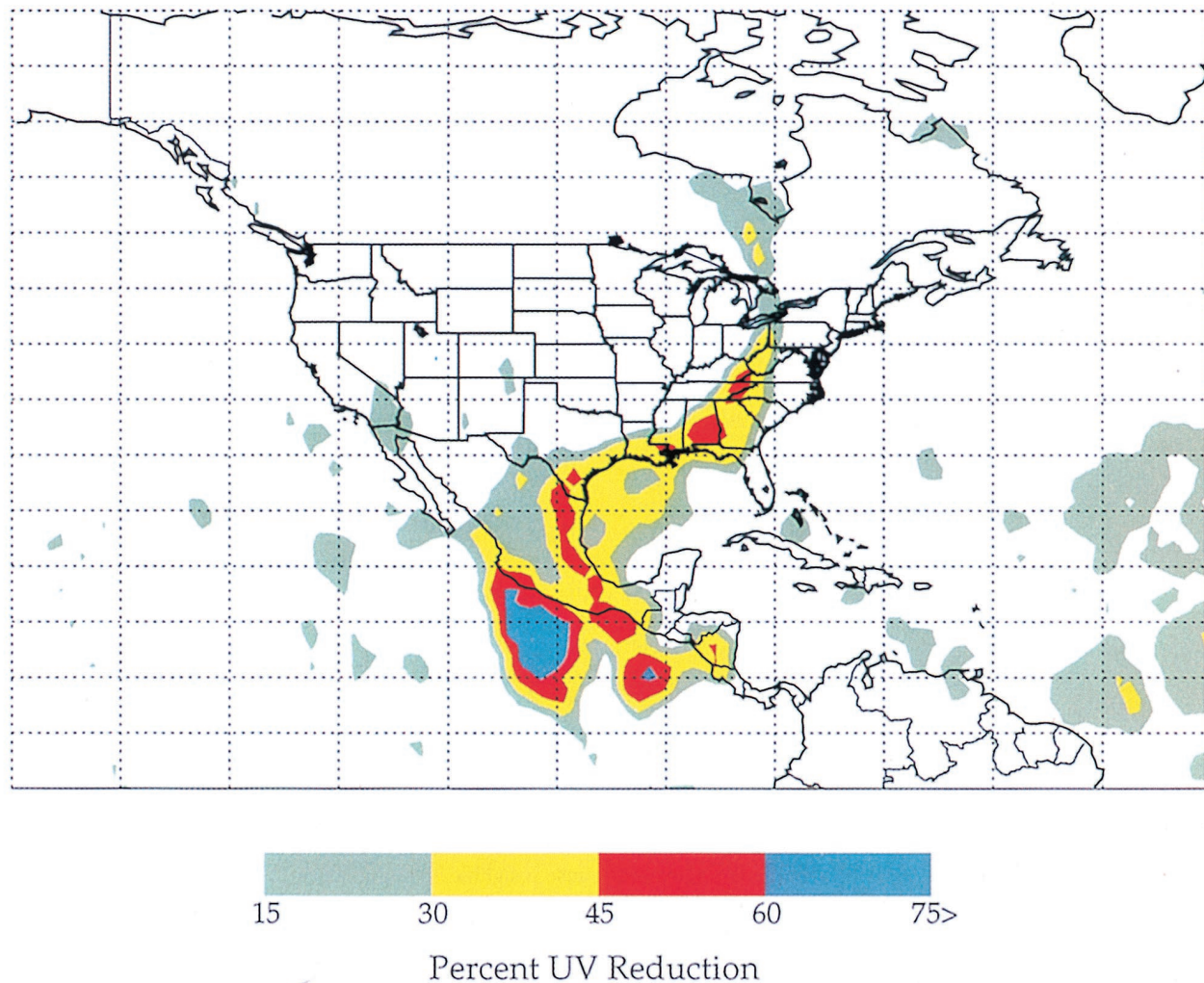
Plate 4. Reduction of UV (May 16, 1998) over Mexico and the southern United States (Florida, Georgia, and Texas) caused by smoke originating in Chiapas, Mexico. An extended plume reached Canada on this day.

during the Northern Hemisphere summer (July) the regions of highest exposure are over the Sahara Desert, Arabian Peninsula, Middle East countries, the elevated regions of India, Pakistan, and China, and the southwestern United States. Most of the high-exposure regions are at relatively low altitude but are also mostly free of cloud cover during July (Plate 1c). In the southwestern United States the high exposures result from a combination of clear skies and moderate elevations. For these months, there is considerable haze and clouds over the ocean areas, since the Intertropical Convergence Zone (ITCZ) cloud region has moved toward the north, so high-exposure areas are not produced over the oceans as they are in the clear-sky Southern Hemisphere. Because of less cloud cover, UV exposures are higher during the Southern Hemisphere summer than in the Northern Hemisphere summers at comparable latitudes.

For latitudes near the tropical regions (±23°) the Sun is at low SZA for months near the equinoxes in March (Plate 1b) and September (Plate 1d). The only UV-irradiance differences between the two equinox months arise from differences in cloudiness and aerosol amounts. On average, the amount of

cloudiness in September exceeds that in March in the latitudes near the subsolar point; that is, in March the ITCZ is still south of the equator, leaving the areas just north of the equator relatively cloud free. In September the ITCZ is still north of the equator, and clouds cover most of the oceans and land near the equator.

As can be seen from the March plate (1b), the exposure levels are very high throughout the horn of Africa region, across the Arabian Sea, southern India, the Bay of Bengal, Malayasia, and parts of Indonesia and the Philippines. In the Western Hemisphere the high-exposure regions are concentrated over Venezuela and Colombia, the West Indies, and southern Central America. Because of the shift in cloud cover, the result is that exposure to UV irradiance is greater in March than in September over most of the equatorial zone. The general features of the geographic UV-exposure distribution with season are largely repeatable from year to year with only small shifts in the overall pattern of high-exposure regions.

Most of the significant aerosol reductions occur in the region covered with dust plumes, and in the regions in southern Africa and South America during the months when there is significant

biomass burning. As shown by *Herman et al*. [1997], the smoke and dust plumes occur annually with moderate interannual variability. The largest year-to-year variability occurs in the South American biomass burning (mostly in Brazil) where there has been an increasing number of fires set for the clearing of land. Additional variability arises from annual changes in the amount of rainfall. In Brazil, increases in the amount and duration of rainfall reduce the amount of fires and accompanying smoke, while in southern Africa, increased rainfall can lead to additional plant growth and increased amounts of biomass burning. From June to September the aerosol dust plumes in the latitude range from 0° to 10°N cover the land and oceans from the Caribbean to the Arabian Sea on many days out of each month [*Herman et al*., 1997]. The dust activity during the months from November to April is much less. Smaller areas are covered by smoke plumes from biomass burning in equatorial and southern Africa and central South America (Brazil) during their dry seasons.

The amount of absorbing aerosols for each different aerosol type and region has a strong seasonal dependence that depends on local meteorological conditions of wind strength and rainfall. The amount of smoke peaks during the regional dry seasons when fields and/or forests are ignited for the purpose of clearing land. The Saharan dust amount has a maximum in the late Northern Hemisphere summer, August and September, and a minimum in December (see the time series in the work of *Herman et al*. [1997]). Using (3), $100(1 - F_A/F_S)$ will have maxima and minima in proportion to the aerosol amounts. Plate 2a shows the average UV-irradiance attenuation (in percent) for the month of January. The most intense reductions (48%, yellow) are from regions of biomass burning with smaller UV-irradiance reductions from dust near 20°N. Some of the smoke from the biomass burning crosses the Atlantic Ocean all the way to the South American coast south of the equator ($-10°$S). There are also smaller amounts of UV-irradiance reduction over the Arabian Peninsula of about 16–20%. Away from the very intense UV reductions near the smoke sources, there are large regions where the reduction ranges from 16 to 24%.

There is a band of aerosols extending around most of the world associated with the specific aerosol sources in each of the months shown. In January, smoke plumes from the biomass burning in equatorial Africa are carried south and westward by low-altitude winds (about 3 km). From there the smoke aerosols are carried across the Atlantic and Pacific Oceans. A similar strong aerosol band occurs for the Saharan dust in July. Weaker but distinct bands occur in other months (e.g., see March and September) with the minimum occurring in November and December when the aerosol activity is at a minimum worldwide. The UV reduction under these extended plumes is about 15 to 20% relative to clear-sky conditions.

Plate 2b shows the UV-exposure reduction in March 1988 caused by a mixture of biomass burning and dust. The intensity of the dust source near 20°N has increased with UV-exposure reductions reaching as high as 48% over small regions in both the Sahara (near Lake Chad and parts of Algeria near 20°N, 0°E) and the Arabian Peninsula. There is a plume of dust coming from the Sahara region and extending nearly to the coast of Spain and another across the Atlantic to South America. During April and May the dust effect intensifies, causing reductions in the Lake Chad region of 50–60%. There are smaller absorbing aerosol reductions in UV exposure (20–30%) which occur over the Arabian Peninsula, the Himalayan

Mountains, portions of India and China. The reductions in China are associated with some of the desert regions and also in the eastern coastal regions near Japan and Korea. June shows a further increase in dust-related UV reductions over the same regions.

Plate 2c shows the UV-exposure reductions in July 1988 caused almost entirely by dust with the maximum UV-exposure reduction reaching 75% over the western Sahara and Sahel. June and July are the months of maximum dust activity, with dust plumes covering northern Africa, the Middle East, sporadic plumes into southern Europe, and plumes over India and China. The dust plumes extend out over the Atlantic Ocean and reach the Caribbean, causing reductions of 16–25% in UV exposure. Small amounts of African dust are present on the east coast of the United States, producing only a few percent reduction. The TOMS dust distributions and seasonal time dependence are consistent with the ground-based observations of dust off the African coast (Tenerife), in the Caribbean, and in Florida [*Chiapello et al*., 1999]. In addition to the dust plumes, there is a small region of UV-exposure reduction from biomass burning in western equatorial Africa which starts in June and reaches a maximum in August.

Plate 2d shows the UV-exposure reductions in September 1988 caused by both biomass burning in Africa and South America as well as from African and Middle East dust. The South American biomass burning shows exposure reductions from 30 to 50%, with 30% over an extended area under the smoke plume as it is transported southward from Brazil by the prevailing winds. While not of the magnitude of the African exposure reductions, there is a moderate UV-exposure reduction caused by absorbing aerosols over large parts of the United States and southern Canada, and in northern Canada during the annual boreal fire season.

While not so important as the effect of clouds, aerosols cause a significant reduction in UV irradiance over very large regions of the Earth for many days (in some cases, for example, desert dust, for months). Under some aerosol plumes the UV irradiance is almost extinguished at the Earth's surface (e.g., the 1997–1998 Indonesian fires (see Plate 3) and 1998 fires in Mexico and Guatemala (see Plate 4)). Because of the wavelength dependence of the aerosol absorption coefficients, the strong absorption of solar radiance does not extend into the visible and longer-wavelength regions. For these wavelengths, there is a smaller reduction in irradiance reaching the surface for the same aerosol plume compared to that for UV wavelengths. Exceptions to this are under the very dense black smoke plumes, occurring in the regions of biomass burning, where the amount of visible light is reduced substantially in the same manner as the UV radiance.

5. Summary

Estimations of the geographical distribution of UV irradiances can be obtained from TOMS satellite data (ozone amount, surface reflectivity, scene reflectivity (clouds and scattering aerosols), and absorbing aerosol amounts) when combined with high-resolution extraterrestrial solar radiance measurements (e.g., from ATLAS-3 SUSIM). The results for monthly averaged, erythemally weighted UV irradiance show large regions of very high exposure in the Southern Hemisphere summer (e.g., January), near the equator during March, and to a lesser extent in the Northern Hemisphere summer (e.g., July). The high-exposure regions follow the seasonal sub-

solar point except during a period near September when clouds from the ITCZ region reduce the amount of UV in the equatorial region (e.g., relative to March). Populated regions with the highest summer exposure to UV irradiance are in Australia and South Africa, where clear-sky conditions generally prevail. The amount of monthly exposure in latitude bands near the subsolar point is determined by the number of cloudy days and, to a lesser extent, by the amount of absorbing aerosols present. In the regions (Africa, South America, and Middle East) where large amounts of absorbing aerosols are present (dust and smoke) the reduction in UV irradiance frequently exceeds $50 \pm 12\%$ of the clear-sky value. In some instances, such as the Indonesian fires during September 1997, the reduction is greater than 90% over a moderately large fraction of the Indonesian-Malaysian land area. Where available, ground-based Sun photometer data show similar UV-irradiance reductions caused by absorbing aerosol plumes of dust and smoke.

Uncorrected comparisons with the Toronto-Brewer data show a systematic bias, with weekly averages from TOMS about 20% larger than weekly averages of Brewer irradiances during the summer months. Examination of major systematic errors between the two data sets (e.g., Brewer cosine error, +6%; model slit-function error, −5%; TOMS nonabsorbing aerosol error, −3%; and TOMS-absorbing-aerosol error, −8%) indicates that the measurements are in as close agreement as possible within the intrinsic instrument errors (±5%, Brewer; ±4.5%, TOMS). Comparisons of irradiance ratios, $I_\lambda/I_{322.5}$ (320–325 nm) between the TOMS and the Brewer spectroradiometers show a residual wavelength-dependent difference that results from an apparent TOMS 2.8% underestimate of the ozone amount over the Toronto Brewer site. When estimating irradiances at the ground from TOMS data, the Toronto-Brewer-related errors are not present.

The accuracy of the TOMS monthly average irradiance estimates are within ±6% except under UV-absorbing aerosol plumes where the accuracy is within ±12%. If the aerosol plume height is better known, the error can be reduced. The daily irradiance values at a given location show the short-term variability (daily to annual) in the amount of UV radiation, 300–400 nm, reaching the Earth's surface caused by partially reflecting cloud cover, ozone, haze, and absorbing aerosols (dust and smoke). After clouds the second largest cause of UV-irradiance reductions, relative to clear-sky irradiances, is caused by the presence of absorbing aerosols over wide areas of the Earth's surface. The largest short-term variations in ozone amount, occurring at high latitudes in the range ±65°, cause changes in UV irradiance comparable to clouds and aerosols only at the shortest wavelengths able to reach the Earth's surface, 280–300 nm, where the amount of radiation is also the smallest, but where the biological sensitivities are maximum for many processes. For a given location the largest monthly cumulative exposures to ultraviolet radiation occur when the Sun is most nearly overhead and when the average amount of cloud cover is at a minimum. Even though terrain height is a major factor in increasing the amount of UV exposure compared to sea level, the presence of prolonged clear-sky conditions can lead to UV exposures at sea level rivaling those at cloudier higher altitudes. For example, a large region for high UV erythemal exposure exists over the ocean near the western coast of Chile and Peru which is comparable to exposures in lower parts of the Andes Mountains. An exception to the maximum erythemal exposure corresponding to overhead Sun conditions occurs in southern Argentina and Chile during the spring when very low ozone amounts pass overhead arising from the Antarctic ozone hole depletion.

Appendix

The UV irradiance at the ground can be estimated from a calculation of the direct beam attenuation and equations (1)–(3) using the following polynomial approximations to the very large radiative transfer tables used for this study. These are less accurate than the tabulated values derived from the radiative transfer equation but are convenient for many applications. Use of these equations is based on the fact that D_{IF} is nearly independent of the ozone amount for a wide range of conditions.

The curves in Figure 2 are represented by the following fitting functions ($\Omega = 375$ DU):

$$\Gamma(0°) = 0.70648 + 0.00744y - 0.00061y^2$$
$$+ 7.338 \times 10^{-6}y^3 \qquad \text{s.d.} = 0.004$$

$$\Gamma(10°) = 0.72405 + 0.00744y - 0.00062y^2$$
$$+ 7.453 \times 10^{-6}y^3 \qquad \text{s.d.} = 0.004$$

$$\Gamma(20°) = 0.78220 + 0.00735y - 0.00065y^2$$
$$+ 7.803 \times 10^{-6}y^3 \qquad \text{s.d.} = 0.004$$

$$\Gamma(30°) = 0.90174 + 0.00666y - 0.00068y^2$$
$$+ 8.326 \times 10^{-6}y^3 \qquad \text{s.d.} = 0.005$$

$$\Gamma(40°) = 1.14025 + 0.00352y - 0.00069y^2$$
$$+ 8.578 \times 10^{-6}y^3 \qquad \text{s.d.} = 0.006$$

$$\Gamma(50°) = 1.68891 - 0.01167y - 0.00039y^2$$
$$+ 5.110 \times 10^{-6}y^3 \qquad \text{s.d.} = 0.008$$

$$\Gamma(60°) = 3.60001 - 0.12697y + 0.00357y^2$$
$$- 5.000 \times 10^{-5}y^3 \qquad \text{s.d.} = 0.05$$

$$\Gamma(70°) = 0.17611 + 33.05e^{-y/1.153}$$
$$+ 14.47e^{-y/3.368} + 9.173e^{-y/33.66} \qquad \chi^2 = 0.07$$

(A1)

where $y = \lambda - 300$ nm, λ = wavelength (nm), s.d. = standard deviation, and χ^2 = chi-square measure of fit.

$$S_b = 0.301173 + 0.011689867y - 4.073496 \times 10^{-4}y^2$$
$$+ 3.95465 \times 10^{-6}y^3 \qquad \text{s.d.} = 0.0026 \qquad \text{(A2)}$$

When the ground is elevated (pressure < 1013 mbar), D_{IF} is reduced as the altitude increases. The ratio R_{DIF} of $D_{IF}(h)$ at some altitude h to $D_{IF}(h = 0)$ at 1013 mbar also decreases with increasing solar zenith angles and with decreasing wavelengths; that is, R_{DIF} decreases with increasing scattering optical path. For small SZA, D_{IF} decreases by about 15% per kilometer altitude. For an estimate of the clear-sky UV irradiance at some altitude between ground and 5 km for solar zenith angles between 0° and 40°, the following approximations can be used with an accuracy of about 5%.

$$R_{DIF} = 1 - 0.16h + 0.0088h^2 \quad 0 \le h \le 5 \text{ km} \quad 300 \text{ nm}$$

$$R_{DIF} = 1 - 0.16h + 0.0094h^2 \quad 0 \le h \le 5 \text{ km} \quad 310 \text{ nm} \quad (A3)$$

$$R_{DIF} = 1 - 0.15h + 0.0078h^2 \quad 0 \le h \le 5 \text{ km} \quad 340 \text{ nm}$$

References

Bass, A. M., and R. J. Paur, The ultraviolet cross-sections of ozone, I, Measurements, in *Atmospheric Ozone*, edited by C. Z. Zeferos, and A. Ghaz, pp. 606–616, D. Reidel, Norwell, Mass., 1985.

Bates, D. R., Rayleigh scattering by air, *Planet. Space Sci.*, 32, 785–790, 1984.

Bernhard, G. B., and G. Seckmeyer, New entrance optics for solar spectral uv measurements, *Photochem. Photobiol.*, 65, 923–930, 1997.

Brueckner, G. E., et al., The Solar Ultraviolet Spectral Irradiance Monitor (SUSIM) onboard the Upper Atmospheric Research Satellite (UARS), *J. Geophys. Res.*, 98, 10,695–10,711, 1993.

Cebula, R. P., E. Hilsenrath, and M. T. Deland, Middle ultraviolet solar spectral irradiance measurements, 1985–1992, from SBUV/2 and SSBUV instruments, in *The Sun as Variable Star: Solar and Stellar Variations*, edited by J. M. Pap et al., pp. 81–88, Cambridge Univ. Press, New York, 1994.

Cebula, R. P., G. O. Thuillier, M. E. VanHoosier, E. Hilsenrath, M. Herse, G. E. Brueckner, and P. C. Simon, Observations of the solar irradiance in the 200–350 nm interval during the ATLAS I mission: A comparison among three sets of measurements—SSBUV, SOLSPEC, and SUSIM, *Geophys. Res. Lett.*, 23, 2289–2292, 1996.

Chiapello, I., J. R. Herman, J. Prospero, and C. Hsu, Detection of mineral dust over the North Atlantic Ocean, and Africa with the Nimbus 7/TOMS, *J. Geophys. Res.*, in press, 1999.

Dave, J. V., Meaning of successive iteration of the auxiliary equation in the theory of radiative transfer, *Astrophys. J.*, 140, 1292–1303, 1964.

Dave, J. V., Multiple scattering in a non-homogeneous, Rayleigh atmosphere, *J. Atmos. Sci.*, 22, 273–279, 1965.

Dave, J. V., and J. Gazdag, A modified Fourier transform method for multiple scattering calculations in a plane parallel Mie atmosphere, *Appl. Opt.*, 9, 1457–1466, 1970.

Eck, T. F., P. K. Bhartia, P. H. Hwang, and L. L. Stowe, Reflectivity of Earth's surface and clouds in ultraviolet from satellite observations, *J. Geophys. Res.*, 92, 4287–4296, 1987.

Eck, T. F., P. K. Bhartia, and J. B. Kerr, Satellite estimation of spectral UVB irradiance using TOMS derived total ozone and UV reflectivity, *Geophys. Res. Lett.*, 22, 611–614, 1995.

Fioletov, V. E., J. B. Kerr, and D. I. Wardle, The relationship between total ozone and spectral UV irradiance from Brewer spectrophotometer observations and its use for derivation of total ozone from UV measurements, *Geophys. Res. Lett.*, 24, 2705–2708, 1997.

Frederick, J., and D. H. Lubin, The budget of biologically active ultraviolet radiation in the Earth-atmosphere system, *J. Geophys. Res.*, 93, 3825–3832, 1988.

Green, A. E. S., The penetration of ultraviolet radiation to the ground, *Physiol. Plant*, 58, 351–359, 1983.

Herman, J. R., and E. A. Celarier, Earth surface reflectivity climatology at 340 nm to 380 nm from TOMS data, *J. Geophys. Res.*, 102, 28,003–28,011, 1997.

Herman, B. M., W. Asous, and S. R. Browning, A semi-analytic technique to integrate the radiative transfer equation over optical depth, *J. Atmos. Sci.*, 37, 1828–1838, 1980.

Herman, B. M., T. R. Caudill, D. E. Flittner, K. J. Thome, and A. Ben-David, Comparison of the Gauss-Seidel spherical polarized radiative transfer code with other radiative transfer codes, *Appl. Opt.*, 34, 4563–4572, 1996.

Herman, J. R., R. Hudson, R. McPeters, R. Stolarski, Z. Ahmad, X.-Y. Gu, S. Taylor, and C. Wellemeyer, A new self-calibration method applied to TOMS/SBUV backscattered ultraviolet data to determine long-term global ozone change, *J. Geophys. Res.*, 96, 7531–7545, 1991.

Herman, J. R., P. K. Bhartia, O. Torres, C. Hsu, C. Seftor, and E. Celarier, Global Distribution of UV-absorbing aerosols from Nimbus-7/TOMS data, *J. Geophys. Res.*, 102, 16,911–16,922, 1997.

Hsu, N. C., J. R. Herman, O. Torres, B. N. Holben, D. Tanre, T. F. Eck, A. Smirnov, B. Chatenet, and F. Lavenu, Comparisons of the TOMS aerosol index with Sun photometer aerosol optical thickness, *J. Geophys. Res.*, in press, 1999.

Kerr, J. B., and C. T. McElroy, Evidence for large upward trends of ultraviolet-B radiation linked to ozone depletion, *Science*, 262, 1032–1034, 1993.

Krotkov, N. A., P. K. Bhartia, J. R. Herman, V. Fioletov, and J. Kerr, Satellite estimation of spectral surface UV irradiance in the presence of tropospheric aerosols, 1, Cloud-free case, *J. Geophys. Res.*, 103, 8779–8793, 1998.

Krotkov, N., J. R. Herman, P. K. Bhartia, Z. Ahmad, and V. Fioletov, Satellite estimation of spectral surface UV irradiance, 2, Effect of horizontally homogeneous clouds, *J. Geophys. Res.*, in press, 1999.

Lean, J. L., G. J. Rottman, H. L. Kyle, T. N. Woods, J. R. Hickey, and L. C. Puga, Detection and parameterization of variations in solar middle and near-ultraviolet radiation (200–400 nm), *J. Geophys. Res.*, 102, 29,939–29,956, 1997.

Lubin, D., and E. H. Jensen, Effects of clouds and stratospheric ozone depletion on ultraviolet radiation trends, *Nature*, 377, 710–713, 1995.

Lubin, D., and E. H. Jensen, Satellite mapping of solar ultraviolet radiation at the Earth's surface, in *Solar Ulatraviolet Radiation: Modeling, Measurements, and Effects*, *NATO Adv. Stud.*, *Inst. Ser I*, vol. 52, edited by C. S. Zerefos and A. F. Bais, pp. 95–118, Springer-Verlag, New York, 1997.

Lubin, D., E. H. Jensen, and H. P. Gies, Global surface ultraviolet radiation climatology from TOMS and ERBE data, *J. Geophys. Res.*, 103, 26,061–26,092, 1998.

Madronich, S., The atmosphere and UV-B radiation at ground level, in *Environmental UV Photobiology*, edited by A. R. Young et al., pp. 1–39, Plenum, New York, 1993.

Mateer, C. L., On the information content of Umkehr observations, *J. Atmos. Sci.*, 22, 370–381, 1965.

McKinlay, A. F., and B. L. Diffey, A reference action spectra for ultraviolet induced erythema in human skin, in *Human Exposure to Ultraviolet Radiation: Risks and Regulations*, edited by W. R. Passchier and B. M. F. Bosnajakovich, pp. 83–87, Elsevier, New York, 1987.

McPeters, R. D., S. M. Hollandsworth, L. E. Flynn, J. R. Herman, and C. J. Seftor, Long-term ozone trends derived from the 16-year combined Nimbus 7/Meteor 3 TOMS version record, *Geophys. Res. Lett.*, 23, 3699–3702, 1996.

Meerkoetter, R., B. Wissinger, and G. Seckmeyer, Surface UV from ERS-2/GOME and NOAA/AVHRR data: A case study, *Geophys. Res. Lett.*, 24, 1939–1942, 1997.

Torres, O., P. K. Bhartia, J. R. Herman, and Z. Ahmad, Derivation of aerosol properties from satellite measurements of backscattered ultraviolet radiation, Theoretical basis, *J. Geophys. Res.*, 103, 17,099–17,110, 1998.

United Nations Environmental Programme (UNEP), *Environmental Effects of Stratospheric Ozone Depletion—1994 Assessment*, edited by J. C. van der Leun, A. H. Teramura, and M. Tevini, Nairobi, 1995.

Woods, T. N., et al., Validation of the UARS solar ultraviolet irradiances: Comaparison with the ATLAS 1 and 2 measurements, *J. Geophys. Res.*, 101, 9541–9569, 1996.

———————

E. Celarier, Software Corporation of America, Beltsville, MD 20705.

J. R. Herman, Laboratory for Atmospheres, Goddard Space Flight Center, Code 916, Greenbelt, MD 20771. (herman@tparty.gsfc.nasa.gov)

N. Krotkov, G. Labow, and D. Larko, Raytheon ITSS Corporation, Lanham, MD 20706.